We are IntechOpen,
the world's leading publisher of
Open Access books
Built by scientists, for scientists

4,800
Open access books available

122,000
International authors and editors

135M
Downloads

Our authors are among the

154
Countries delivered to

TOP 1%
most cited scientists

12.2%
Contributors from top 500 universities

BOOK CITATION INDEX INDEXED
CLARIVATE ANALYTICS

WEB OF SCIENCE™

Selection of our books indexed in the Book Citation Index
in Web of Science™ Core Collection (BKCI)

Interested in publishing with us?
Contact book.department@intechopen.com

Numbers displayed above are based on latest data collected.
For more information visit www.intechopen.com

Laser-based Particle Acceleration

Hans-Peter Schlenvoigt[1,2], Oliver Jäckel[1],
Sebastian M. Pfotenhauer[1,3], and Malte C. Kaluza[1]
[1]IOQ, Friedrich-Schiller-Universität, Jena,
[2]LULI, École Polytechnique, Palaiseau,
[3]MIT, Cambridge, MA,
[1]Germany
[2]France
[3]United States

1. Introduction

The acceleration of charged particles relies on the use of longitudinal electric fields. These fields are typically generated either via capacitors as static electric fields, or via microwaves carried in resonators. Accelerator devices of this sort are, however, constrained by their material damage thresholds: If the electric field in the cavities exceeds ~ 50 MV/m, conduction band electrons from the material are field-ionized, leading to a breakdown of the accelerator. As a consequence, the energy gain per unit length in conventional accelerators is limited, and high particle energies can only be realized through additional acceleration length, which explains the sometimes impressively large dimensions of state-of-the-art accelerators.

This chapter is dedicated to a radically new approach towards particle acceleration based on laser-produced plasma. In contrast to conventional accelerator cavities, plasmas can generate and support electric fields up to TV/m. In the present case, the plasma is created by an ultra-short, ultra-intense laser pulse impinging on a target, whereupon the free particles interact immediately with the strong electromagnetic fields of the laser. Since the energy density of such ultra-short pulses is extremely high, efficient energy coupling processes exist between the laser field and the plasma, and the particle may gain substantial kinetic energy within very short distances. As of today, laser-plasma accelerators are capable of producing beams of 1 GeV electron energy over 3 cm of acceleration length (Leemans et al., 2006; Karsch et al., 2007), as well as ion beams of several 10 MeV per nucleon over a distance of some ten microns (Snavely et al., 2000). These laser-produced particle beams possess a number of outstanding properties, such as ultra-short pulse duration of the order of the laser pulse (Pukhov & Meyer-ter-Vehn, 2002; van Tilburg et al., 2006; Fuchs et al., 2006), high peak currents and excellent emittance values (Cowan et al., 2004). Given these unique beam properties and the compactness of the acceleration scheme, the field of laser-based particle acceleration has recently attracted much attention for its great potential for exciting new applications in fundamental and applied physics.

The present chapter will be organized as follows: First, we briefly review the principle of chirped pulse amplification as the fundamental optical technology underlying the

generation of ultra-intense laser pulses, as well as some fundamentals of ionization processes at high intensities. We then present the central mechanisms of laser-matter interactions at ultrahigh intensities, such as nonlinear Thomson scattering, the ponderomotive force and plasma heating processes. The main part of this chapter will be devoted to a detailed description of laser-based acceleration processes, both for electrons ("Laser Wake-Field Acceleration") and ions ("Target Normal Sheath Acceleration"). Particular attention will thereby be paid to the generation of quasi-monoenergetic particle pulses with relatively moderate experimental requirements, which is an essential prerequisite for almost all applications. The final section will discuss a number of potential applications for laser particle accelerators. These include the production of short-pulsed synchrotron radiation from laser-accelerated electrons passing through an undulator as well as other small scale radiation sources for structural analysis, the possibility of laser-based radiation therapy in oncology, and applications in high energy-density physics like astrophysical studies or laser-based fusion energy sources.

2. Fundamentals of laser-plasma-physics

2.1 High-intensity laser systems

Ultra-high light intensities are produced by releasing a certain amount of laser energy W_L in a very short time span τ_L and focusing it to a very small spot size A_{foc}:

$$I_L = \frac{W_L}{\tau_L \cdot A_{foc}}. \tag{1}$$

Today's state-of-the-art laser system are capable of applying about 8 Joules of energy within a pulse duration of 30 fs and a focus area of about 5 μm, achieving intensities in excess of 10^{20} W/cm² while still fitting on one optical table. These intensities are equivalent to all the sun light reaching the earth surface, focused on the tip of a pencil. At present, the only technique capable of generating such intensities is the the so-called *Chirped Pulse Amplification* (CPA) (Strickland & Mourou, 1985). A mode-locked, dispersion-compensated optical oscillator generates ultra-short but spectrally broad laser pulses with pulse durations as short as $\tau_L \sim 10$ fs. These pulses contain initially only Nanojoules of energy. In order to amplify them without damaging the amplifier by too high pulse powers or intensities, the pulses are at first temporally stretched with help of dispersing elements by imprinting a positive chirp (which is equivalent to 2nd-order dispersion) onto the pulse. This easily leads to stretched pulse durations of 100's of ps. Subsequently, the long and less powerful pulses are amplified to several Joules. In order to re-compress them afterwards to ultra-short durations, all spectral components must experience the same gain during the amplification process. This condition restricts the available laser media to only a few ones like Ti:Sapphire, Nd:Glass, Yb:FP-Glass or Yb:CaF₂ and therefore the laser wavelengths λ_L to the near-infrared range. Finally, the pulses are re-compressed to ultra-short pulse durations by applying the inverse dispersion. The resulting pulses then have multi-TW to PW power and would interact with any transmissive material. Hence, only reflective elements are allowed and the beam must be guided in vacuum.

In order to obtain ultra-high intensities, these high-power laser pulses are focused with off-axis parabolic mirrors. For a given laser facility, degrees of freedom are mainly the pulse energy (since the amplification can be easily controlled) and the focal spot size (determined

by the focusing optic). The pulse duration can easily be increased by detuning the pulse compressor (reducing the final pulse power), but reducing the pulse duration below a certain level, determined by the laser system or — more precisely — the spectral bandwidth of the amplified pulses, is usually not possible.

2.2 Ionization

Peak intensities necessary for laser-based particle acceleration are above $I_L \sim 10^{18}$ W/cm², which constitutes the so-called "relativistic threshold" for near-infrared wavelengths. Under such conditions, the primary mode of interaction between electromagnetic waves and matter is no longer resonant excitation of atomic states, but any material is readily ionized through *multi-photon-*, *tunnel-* and *optical-field-ionization* (Gibbon, 2005). For the laser pulses under consideration, ionization occurs already during the rising edge of the laser pulse, when the intensities exceed the range of $I_L \sim 10^{10}$ W/cm². In the multi-photon-regime, several photons are absorbed by the atom within a time period shorter than the relaxation time of the virtual excitation state. Hence, the photon energies add and appear like a single energetic photon. In the tunnel- and field-ionization regimes, the laser's electric field amplitude is comparable to the binding Coulomb field of the nucleus. Bound electrons can either tunnel through the finite potential well, formed by the superposition of the external laser field and the Coulomb field, or the potential well is completely suppressed and electrons are released into the vacuum instantaneously.

2.3 Plasma properties

Among the most important properties of plasma are its ability to screen charges, to support oscillations of the electron distribution against the positively charged ion background, and to react quickly on electromagnetic fields. These features arise mainly from the plasma's composition of quasi-free light electrons and heavy ions. Ions are usually treated as immobile, only electrons will react on internal or external electromagnetic fields.

The fundamental parameters of a plasma are its *electron density* n_e and *electron temperature* T_e. The temperature is usually defined via the mean kinetic energy of the electrons, $T_e = \langle W_{kin} \rangle / k_B$. Note that even a non-Maxwellian energy distribution yields a certain value of T_e. A first deduced quantity is the electron *plasma frequency*

$$\omega_p = \sqrt{\frac{e_0^2 n_e}{\varepsilon_0 m_e}} \tag{2}$$

which characterizes oscillations of electrons around the immobile ions in case of a certain displacement from the equilibrium position. A second important deduced quantity is the *Debye length*

$$\lambda_D = \sqrt{\frac{\varepsilon_0 k_B T_e}{e_0^2 n_e}} \tag{3}$$

which describes the distance after which the potential of a local charge density perturbation is reduced to $1/e$ of its initial value. Here, e_0 is the electron charge, m_e the electron rest mass, ε_0 the permittivity of free space and k_B the Boltzmann constant and e Euler's number.

The propagation of light with frequency ω_L and wave number $k_L = 2\pi/\lambda_L$ is determined by the dispersion relation

$$\omega_L^2 = \omega_p^2 + k_L^2 c^2 \; , \tag{4}$$

where c is the speed of light. Electromagnetic waves cannot propagate in plasma if $\omega_L \leq \omega_p$. The limit $\omega_L = \omega_p$ corresponds to a maximum electron density called *critical density*,

$$n_c = \frac{\varepsilon_0 m_e \omega_L^2}{e_0^2} = \frac{\varepsilon_0 m_e 4\pi^2 c^2}{e_0^2 \lambda_L^2}, \tag{5}$$

which must not be exceeded to allow light propagation in the plasma. Plasma with electron densities $n_e < n_c$ are called *underdense*, otherwise *overdense* plasma.
Due to the dispersion relation (4), the plasma has an *index of refraction*

$$\eta = \sqrt{1 - \frac{\omega_p^2}{\omega^2}} = \sqrt{1 - \frac{n_e}{n_c}} < 1 . \tag{6}$$

For dilute plasma, $n_e \ll n_c$, Eq. (6) may be approximated by $\eta \approx 1 - 0.5 \, n_e/n_c$.

2.4 Relativistic motion of single electrons
The motion of electrons in electromagnetic fields is described by the Lorentz force,

$$\frac{d\mathbf{p}}{dt} = -e_0(\mathbf{E}(\mathbf{r}) + \dot{\mathbf{r}} \times \mathbf{B}(\mathbf{r})), \tag{7}$$

where $\mathbf{p}(t) = \gamma m_e \dot{\mathbf{r}}(t)$ is the relativistic electron momentum, γ the relativistic Lorentz factor $\gamma = (1 - \dot{\mathbf{r}}^2/c^2)^{-1/2} = [1 + \mathbf{p}^2/(m_e c)^2]^{1/2}$, $\mathbf{E}(\mathbf{r}, t)$ the electric and $\mathbf{B}(\mathbf{r}, t)$ the magnetic field at the electron's actual position $\mathbf{r}(t)$ and $\dot{\mathbf{r}}(t)$ the electron velocity.
As a start, let's consider the motion in an infinite, plane electromagnetic wave, linearly polarized in the x-z-plane and propagating in z-direction, $\mathbf{E}(\mathbf{r}, t) = \hat{\mathbf{x}} E_0 \sin(kz - \omega t)$. We replace the electric field amplitude by the amplitude of the *normalized vector potential*,

$$a_0 = \frac{e_0 E_0}{m_e \omega c} \approx 0.85 \times \frac{\lambda_L}{\mu m} \times \sqrt{\frac{I_L}{10^{18} \, W/cm^2}} \; . \tag{8}$$

This quantity represents the "relativisticness" of the motion. If $a_0 \ll 1$, one can neglect the influence of the $\dot{\mathbf{r}} \times \mathbf{B}$-term and finds that a_0 is the ratio of the amplitude of the quiver velocity to c. Intensities yielding $a_0 \gtrsim 1$ are called "relativistic intensities" and will be considered in the following.
To solve Eq. (7), we perform a variable transformation, $\tau = t - z(t)/c$, which describes the phase of the wave and is also the proper time t/γ of the electron. Finally, we find

$$x(\tau) = \frac{c a_0}{\omega} \sin(\omega \tau) \tag{9a}$$

$$y(\tau) = 0 \tag{9b}$$

$$z(\tau) = \frac{c a_0^2}{4} \left(\tau + \frac{1}{2\omega} \sin(2\omega \tau) \right). \tag{9c}$$

To the first order of the field amplitude a_0, the electron oscillates with ω parallel to the electric field vector, x. But to second order and thus dominant for relativistic intensities, there is an oscillation with double frequency 2ω combined with a drift motion along the propagation direction of the wave, z. This motion induces a characteristic light emission called *nonlinear Thomson scattering* (Lau et al., 2003).

Figure 1 shows trajectories according to Eq. (9) for an electron, in a frame co-moving with the electron's drift velocity $c\ a_0^2/(4 + a_0^2)$ along the laser propagation direction (a) and (b) in the lab frame, for three different intensities (or vector potential amplitudes a_0). The black curve is for $a_0 = 0.215$ which corresponds at $\lambda = 800$ nm to an intensity of $I = 10^{17}$ W/cm². This is almost a classical linear oscillation. At higher intensities, $a_0 = 0.6$ (green) and $a_0 = 0.96$ (blue), the motion in the co-moving frame becomes a figure-of-8, and the drift motion along the laser propagation direction is more pronounced in comparison to the transverse oscillation. Note that for $a_0 \approx 1$ (blue curve), the drift distance during one laser oscillation in the electron's time frame τ is already a quarter of the laser wavelength, which corresponds to a relativistic average forward velocity and again clearly shows the relativistic character of the motion.
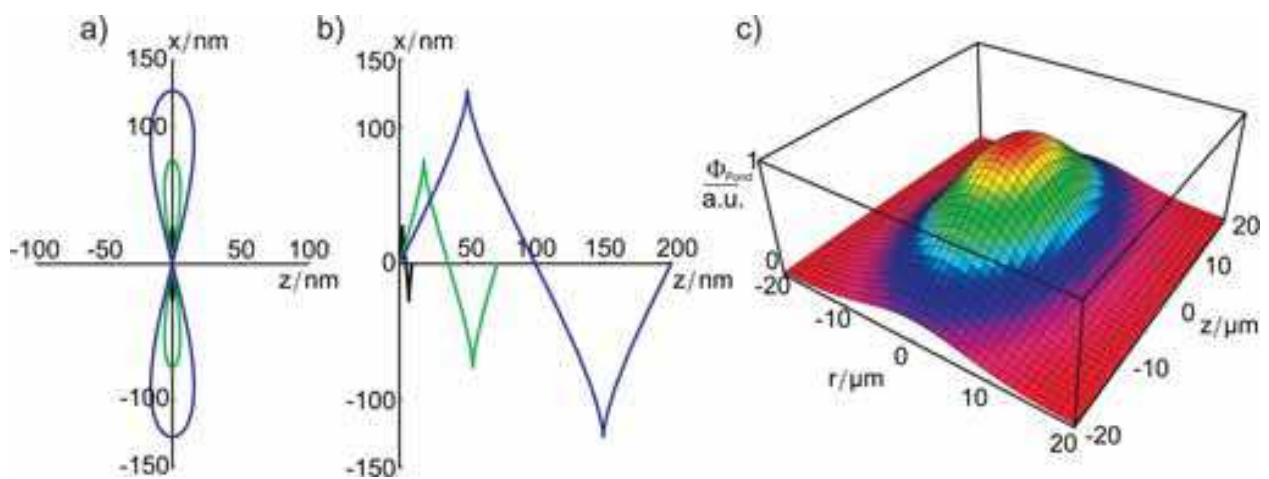

Fig. 1. Electron trajectories in the average rest frame (a) and the laboratory frame (b) of nonlinear Thomson scattering, for different laser intensities and during one laser period experienced by the electron; (c) the ponderomotive potential of a laser pulse of 15 μm full width at half maximum (FWHM) diameter and 85 fs FWHM pulse duration.

2.5 Ponderomotive force

The previously discussed case exhibits no net particle acceleration, caused by the assumption of an infinite plane wave. Even for finite pulse durations, the electron is shifted in forward direction but comes to a rest again after the laser pulse has passed. This is different for focused laser pulses with transverse dimensions and therefore steep *intensity gradients*. Averaging the Lorentz force in time over the fast oscillatory contributions, $\langle \ldots \rangle_T$, i.e. regarding just the pulse envelope, yields the *ponderomotive force* (Kruer, 1988),

$$\mathbf{F}_{\text{Pond}} = \left\langle \frac{d\mathbf{p}}{dt} \right\rangle_T = \frac{-e_0^2}{2m_e\omega^2}\nabla\langle E^2 \rangle_T = \frac{-e_0^2}{2\varepsilon_0 m_e \omega^2 c}\nabla I(\mathbf{r}). \tag{10}$$

The related ponderomotive potential reads as

$$\Phi_{\text{Pond}} = \frac{e_0^2}{2\varepsilon_0 m_e \omega^2 c} I(\mathbf{r}) = \frac{a_0^2}{4} m_e c^2 \ . \tag{11}$$

Figure 1 (c) shows the ponderomotive potential of a laser with 15 μm FWHM diameter and 85 fs FWHM pulse duration. The shape of the ponderomotive potential is effectively dominated by the intensity envelope of the focused laser pulse.

We see that the ponderomotive force creates an effective net push in direction away from high intensities, being proportional to the intensity gradient. This allows electrons to gain net momentum, especially in laser propagation direction. Ponderomotive pressure is one of the key mechanisms for electrons to acquire kinetic energy at relativistic intensities and plays a central role in both electron and ion acceleration.

2.6 Effects at relativistic intensities: Relativistic optics

The previous sections have shown that electrons exposed to relativistic intensities are subject to a relativistic quiver motion and a net force. The first aspect leads — for quantities based on time-scales larger than the laser period — to an effective *relativistic mass increase* of the electrons. Therefore, in Eqs. (2), (5), (6) and (10), the electron rest mass must be replaced by the average relativistic mass, $m_e \mapsto \langle\gamma\rangle_T m_e$. The average relativistic factor is given by $\langle\gamma\rangle_T = (1 + a_0^2/2)^{1/2}$. The second effect, the ponderomotive force, leads to local *changes of the plasma electron density*. The derivation of the correct relativistic ponderomotive potential is a little more complicated (Meyer-ter-Vehn et al., 2001). Solving the equation of motion in consideration of additional plasma fields and currents (not only the laser field), one finds

$$\Phi_{\text{Pond}} = \left(\sqrt{1 + a_0^2} - 1\right) m_e c^2, \tag{12}$$

what is just the electron's relativistic kinetic energy acquired from the laser field. Note that this corresponds to $\Phi_{\text{Pond}} = (\langle\gamma\rangle_T - 1)m_e c^2$ with $\langle\gamma\rangle_T = (1 + a_0^2/2)^{1/2}$ which is slightly different from the formula given above above.

Both effects alter the optical properties of the plasma via Eqs. (2) and (6) at regions where the laser pulse is present. By that, the laser pulse propagation and ultimately the laser pulse shape itself can be altered, too. This mutual interaction leads to a feedback loop (Mori, 1997). Most noteworthy effects in this context are self-focusing and self-modulation.

Self-focusing arises from changes of the refractive index such that at regions at high intensity the refractive index is increased. This leads to a focusing density profile which counteracts natural diffraction and may prolong the interaction region. Self-focusing occurs when the laser pulse power exceeds the following limit: $P_L > P_{SF} \approx n_c/n_e \cdot 17.4$ GW. *Self-modulation* has a similar underlying effect but leads to longitudinal bunching and compression of the laser pulse. It is caused by periodic modulations of the plasma density which arise from the ponderomotive force and the plasma's ability to perform oscillations. Further effects of these *modulation instabilities* are Raman forward scattering, photon acceleration, hosing and filamentation. The name arises from the fact that these effects inhibit stable laser propagation and modulate certain quantities of the laser pulse (Mori, 1997).

2.7 Energy absorption processes

Up to now, an underdense plasma was considered, being a rather transparent and — depending on the intensities — nonlinear medium without significant energy loss. The situation becomes different in case of reaching the critical density, $\omega_L = \omega_p$, or resonance between the laser pulse envelope and the plasma frequency (cf. Sec. 3.1).

Here we consider an interface from vacuum to overdense plasma. The electron density may be modelled by an exponential decay, $n_e(z) = n_{e,0} \cdot \exp(z/L_P)$ for $z < 0$ (in front of the target) and $n_e(z) = n_{e,0}$ for $z > 0$ (inside the target), cf. Fig. 2 (a). The quantity L_P is called *scale length* of the plasma at the target front side. This plasma originates from ionization of the target material by the leading edge of the laser pulse and is called *preplasma*. The steeper the leading edge, the later the preplasma is formed and the steeper the density gradient. The case of $L_P \rightarrow 0$ resembles a perfect step-function-like density gradient. Coming back to the laser-plasma interaction, we find that the plasma shows a high reflectivity at low intensities which is due to the large amount of free charges, similar to a metal mirror. However, at high intensities, significant absorption is observed.

At first sight, one can introduce a damping term into the Lorentz equation of the electron motion that represents *collisions* between laser-influenced electrons and ions. It can be shown that the collision frequency scales like $\nu_{ei} \sim (k_B T_e)^{-3/2}$, accordingly collisional damping becomes less effective for higher electron temperatures what starts at intensities of about 10^{15} W/cm² (Gibbon, 2005). Therefore, other *collisionless* mechanisms have to be taken into consideration. The most relevant collisionless absorption processes are resonance absorption and Brunel heating as well as the already introduced ponderomotive acceleration (cf. Sec. 2.5), which is closely related also to $\mathbf{v} \times \mathbf{B}$ heating.

All processes finally lead to an electron fraction with much higher mean kinetic energy than the residual, unaffected plasma electrons. Hence, these electrons give rise to a *suprathermal* component which is simply called "hot electrons", and the processes are referred to as "heating processes".

Resonance absorption and Brunel heating A *p*-polarized laser pulse with oblique incidence on the target, i.e. $\theta_L > 0$, has an electric field component which is directed parallel to the preplasma gradient. Under oblique incidence, due to the $\mathbf{k}$-vector conservation (Kruer, 1988), reflection actually occurs before the critical density is reached. This implies, that electrons, forced by the laser to oscillate, generally do not match the local plasma frequency in the density profile, cf. Fig. 2. The electron density occurring at the turning point of the incident wave is deduced by $n_{e,refl} = n_c \cos^2 \theta_L$ which is less than the critical density for incidence angles larger than zero.

At the turning point, the electric field component of the incident wave generates a standing wave pattern oscillating in target-normal direction (z). However, in case of a sufficiently small distance between the turning point and the position of the critical density, the evanescent electric field suffices to excite an electron oscillation parallel to the electron-density gradient, i.e. in longitudinal direction, within the region of the critical density. This very localized and quasi-standing plasma wave is resonantly excited by the laser field and can therefore be driven so strongly that it breaks (cf. Sec. 3.1.3). Then, a sufficient number of hot electrons is pushed into the target and transport energy obtained from the laser. This process is called *resonance absorption*. Absorption rates up to $\eta_{abs}^{RA} = 60$ % are reported for optimized laser and plasma parameters (Gibbon, 2005).
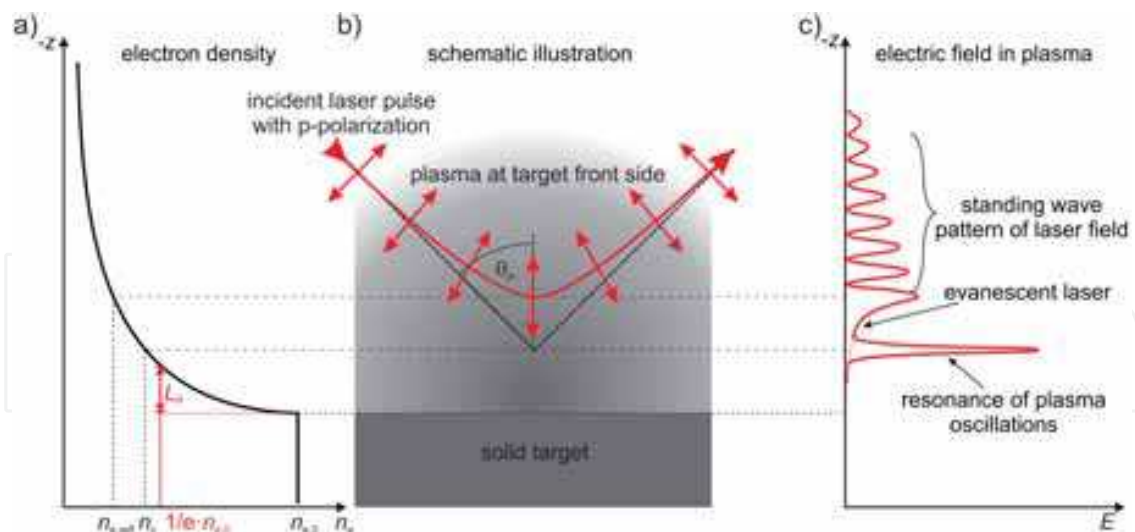
Fig. 2. Reflection at an exponential plasma profile. A *p*-polarized laser pulse obliquely incidences the preplasma profile at the target front. Reflection occurs already before the critical density has been reached. If the distance between the standing wave pattern at the turning point and the position of the critical density is short enough, the evanescent decaying electric field can excite electron oscillations at this position in longitudinal direction (into the target). Since this oscillation is excited resonantly, it can be driven so strongly that it breaks and a sufficient number of hot electrons is pushed inside the target.

Brunel heating, (Brunel, 1987), takes place at very steep plasma gradients and benefits from the fact that the laser penetration depth is smaller than the maximum displacement of the oscillating electrons. The acceleration process now takes place in the vacuum space in front of the preplasma profile or the target, respectively.

During the first half cycle of a laser period, the electrons move away from the target into the vacuum, turn around, and are accelerated back towards the target. But once they enter the target, they soon get screened from the laser fields which again penetrate the plasma only evanescently. By that, the electrons retain most of their kinetic energy and carry laser energy into the plasma. The absorption rate via Brunel absorption just depends on the incidence angle of the laser, the plasma properties are more or less fixed due to the assumption of a very steep plasma gradient. Hence, $\theta_L = 45°$ accords to an absorption rate of $\eta_{abs}^{Brunel} = 60$ %. This very large value has to be discussed rather critically: Firstly, the Brunel mechanism does not account for finite plasma scale lengths, but typical experimental conditions do not reveal a very steep plasma gradient. Furthermore, numerical studies, assuming very short but finite preplasma scale lengths (Gibbon, 2005), show that η_{abs}^{Brunel} saturates at about 10–15 %.

Ponderomotive force and v ×B heating The ponderomotive force allows that electrons from the preplasma can be pushed along the laser propagation direction. However, the laser pulse cannot follow the electrons into overdense regions since it is reflected at the critical density or even before, but electrons remain moving along the initial direction. The mean kinetic energy of the electrons was given by the ponderomotive potential, see Sec. 2.5. Typically, mean kinetic energies of a few MeV can be obtained (Gibbon, 2005).

The last effect to be discussed is $\mathbf{v} \times \mathbf{B}$ heating (Gibbon, 2005). Electrons oscillating in the electric field of a laser pulse with relativistic intensity experience the influence of the $\mathbf{v} \times \mathbf{B}$ term of the Lorentz force as discussed in Sec. 2.4. For steep plasma gradients, this effect can contribute to the absorption rate analogously as the Brunel mechanism does: During the first

(or third) quarter of the optical cycle, electrons are accelerated into the vacuum, turn around, and are accelerated back to the target where they become screened from the electromagnetic wave and retain with their kinetic energy. In contrast to the Brunel mechanism depending only on the electric field of the laser, $\mathbf{v} \times \mathbf{B}$ heating acts along the laser propagation direction due to the magnetic field contribution and not along the polarisation direction. Hence, $\mathbf{v} \times \mathbf{B}$ heating favours small incidence angles of the laser. The kinetic energy achievable via $\mathbf{v} \times \mathbf{B}$ heating is deduced by the a_0^2 -dependence of the electron momentum in longitudinal direction, cf. Eq. (9c). Again, the MeV-range is reached. Due to the relation to the Brunel mechanism, similar absorption rates of 10–15 % are expected after reaching the regime of relativistic intensities (Kruer & Estabrook, 1985).

3. Laser-based electron acceleration

In this section we will point out the physical concept of how a plasma can be used to generate high-energy electron bunches. Although we already presented principles which can transfer energy from the laser to plasma electrons, the generation of high-energy, narrowband and collimated electron beams (similar to those of conventional accelerators) is different. At first, we will introduce the fundamental theoretical model, which is split into different subtypes. Secondly, we will show original experimental data: We will depict a setup, explain the course of action for the production of high-quality electron beams and present characteristics of produced electron beams. Finally, we will describe possible extensions, improvements and potential future developments.

The generation of highly energetic and collimated electron beams happens in a underdense plasma. Therefore, the highly efficient absorption mechanisms (cf. Sec. 2.7) cannot be used. Only the direct interaction of the laser's electromagnetic field with plasma electrons or the ponderomotive force are in action. This leads to 2 physically different regimes of electron acceleration: The *laser wakefield acceleration* (LWFA) (Tajima & Dawson, 1979; Modena et al., 1995) and *direct laser acceleration* (DLA). In the DLA regime (Gahn et al., 1999), a direct energy transfer from the transverse laser fields to a forward electron momentum takes place. However, beams with comparably large divergence angles and broadband spectra can be produced. For that reason we will not discuss DLA.

3.1 The model of Laser Wakefield Acceleration

The LWFA regime (Tajima & Dawson, 1979) relies on two steps:

- An intense laser pulse drives a plasma wave by the ponderomotive force, like a boat generates its wake on the sea. This plasma wave is accompanied by strong electric fields and is co-moving with the laser pulse.
- If electrons are injected at the peak of the wake, they can gain energy from the space charge electric field of the plasma wave, similar to the way a surfer does from an ocean wave.

This regime has different sub-types (Esarey et al., 1996), most important are self-modulated LWFA (SM-LWFA) and bubble acceleration (Pukhov & Meyer-ter-Vehn, 2002), which will be discussed later in Sec. 3.2. All these variants of LWFA are in principle capable of producing collimated electron pulses with narrowband spectra.

Before we go into details it must be noted that the following description of the LWFA regime considers plane plasma waves which corresponds to a 1-dimensional (1D) approach where only variations along the propagation direction are taken into account. This simplifies

the physical picture but is a bit unrealistic since in reality the plasma wave amplitude varies with the radial distance due to the transverse intensity profile of the laser pulse. Those transverse effects are difficult to model analytically but play an important role and will be discussed later in Sec. 3.2.2.

3.1.1 Plasma wave excitation

Let us start by recalling that the ponderomotive force is directed anti-parallel to the intensity gradient, see Eq. (10). Hence, plasma electrons are pushed away from intense laser pulses. Now, consider a laser pulse approaching a certain region in the plasma. Electrons are at first pushed forward. A local charge separation is formed since the ions are not affected by the laser pulse and remain at rest. The electron density changes locally by an amount of δn_e which depends mainly on the laser intensity gradient. Space charge forces start to pull the electrons back. After some time, the laser pulse overtakes the electrons since the forward and back-pointing forces compensate. The electrons will then experience a kick backwards from the ponderomotive force. The density depression becomes compensated by electrons streaming back to the depression. However, the inertia of the moving electrons hinders a stable charge density compensation. Instead, there is an overshoot, and then the electrons swing back and forth. In other words, the laser pulse has excited a plasma oscillation at the considered region, like a guitarist picking a string.

Since the laser pulse moves through the plasma, it excites oscillations all along its path. Furthermore, between the oscillations, there is a certain phase relation given by their individual time of excitation. Therefore, all oscillations together form a *travelling plasma wave* with a phase velocity equal the group velocity of the laser pulse v_{gr}. This is similar to the wave pattern induced by a speedboat, which is also co-moving with the boat. The corresponding wave length of this electron density oscillation is called plasma wavelength and is given by

$$\lambda_p = \frac{2\pi v_{gr}}{\omega_p} \approx \frac{2\pi c}{\omega_p}. \tag{13}$$

The excitation is most effective if the laser pulse fits into the first half-period of the plasma wave (Tajima & Dawson, 1979). This results in the resonance condition

$$\omega_p \cdot \tau_L = \pi. \tag{14}$$

This is a delicate condition, as it relates the laser pulse duration to the electron density via Eq. (2) and therefore puts severe constraints on the experimental conditions.

3.1.2 Nonlinear plasma waves

In the case of strong excitation, the electron density variation may become large, $\delta n_e \sim n_e$. This leads to ultra-high space charge fields in the plasma and relativistic longitudinal quiver velocities of electrons during the plasma oscillations. Hence, the plasma frequency is altered during the oscillation and the oscillation becomes anharmonic as shown in Figure 3. The longitudinal electric field in the excited plasma wave is given by (Esarey et al., 1996)

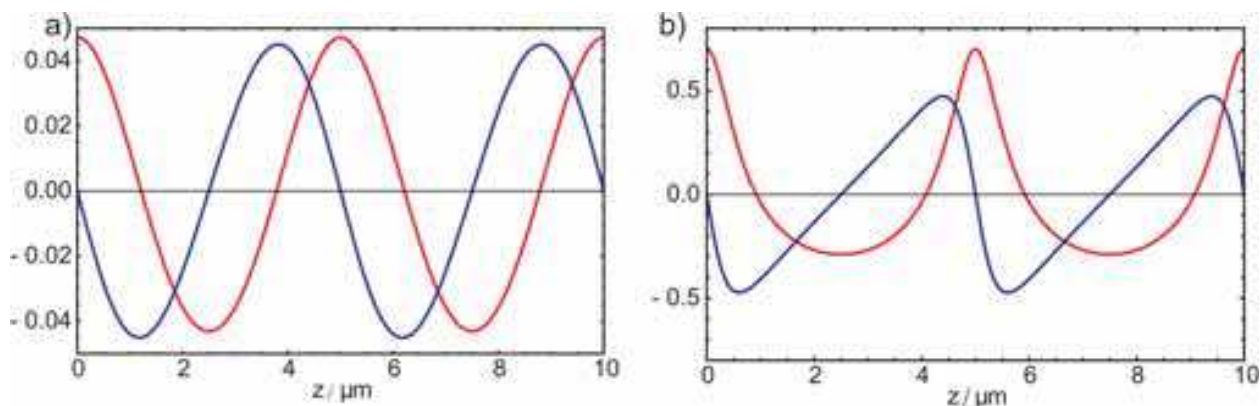$$E_{wake} \approx \frac{a_0^2 / 2}{\sqrt{1 + a_0^2 / 2}} \underbrace{c m_e \omega_p / e_0}_{E_p}. \tag{15}$$

Fig. 3. Electron density perturbation $\delta n_e/n_e$ (red) and longitudinal electric field E_{wake}/E_p (blue) for (a) a weakly relativistic laser pulse ($a_0 \sim 0.3$) and and (b) a relativistically intense pulse ($a_0 \sim 1$) in a plasma with 5 μm plasma wavelength. Calculated according to Sec. 4.1 in (Gibbon, 2005).

3.1.3 Wave-breaking and injection

The plasma wave closely follows the laser pulse and travels almost with the speed of light. As a result, electrons must be injected in the travelling electric field with significant forward velocity in order to be caught by the wave and subsequently to be accelerated further by the field. However, as the velocity of the wave is smaller than c, the electrons can stay in the accelerating region of the plasma wave for a significant period of time and thus gain considerable amounts of kinetic energy. Among several possibilities (see later Sec. 3.4), a simple option for injection is *wave-breaking*.

Wave-breaking occurs when the individual particle velocities within the wave reach the phase velocity of the wave. In low-amplitude plasma waves, electrons just swing back and forth. In large-amplitude waves, however, particles can slip out of the wave, similar to whitecaps at the ocean's surge. Thereby, wave-breaking sets on the one hand the limit of the plasma wave amplitude and the electric fields inside the wave. On the other hand, it happens at the right position of the wake (its maximum) and particle velocities suffice to catch the wave. For this reasons, wave-breaking is called *self-trapping* of electrons. Furthermore, injection of electrons reduces the longitudinal electric fields and can inhibit further electron injection. This is called *beam loading*, which leads to an inherent control of the accelerated electron beam (Geddes et al., 2005).

In a nonlinear plasma wave, the wave-breaking limit limit is given by (Esarey et al., 1996)

$$E_{wb} = \sqrt{2(\gamma_p - 1)} E_p , \qquad (16)$$

where γ_p is the relativistic factor related to the phase velocity of the wake and may be approximated to $\gamma_p \approx \omega_L/\omega_p = \sqrt{n_c/n_e}$. In order to reach wave-breaking, $E_{wake} \geq E_{wb}$, the laser pulse amplitude must significantly exceed the relativistic limit, $a_0^2 \gg 1$:

$$\underbrace{\frac{a_0^2/2}{\sqrt{1 + a_0^2/2}}}_{\approx a_0/\sqrt{2}} \geq \sqrt{2(\sqrt{n_c/n_e} - 1)} . \qquad (17)$$

3.1.4 Energy gain considerations

In general, the acceleration process can be limited by the following processes:

- Diffraction: the laser beam has a finite Rayleigh length
- Depletion: the plasma wave excitation consumes the laser pulse energy
- Dephasing: after some acceleration, electrons move faster than the plasma wave and slip into a decelerating phase.

Diffraction is usually not a problem. The depletion limit can be roughly estimated by equating the initial laser pulse energy to the energy left behind in the plasma wave and is (Esarey et al., 1996)

$$L_{\mathrm{depl}} \sim \frac{n_{\mathrm{c}}}{n_{\mathrm{e}}} \lambda_{\mathrm{p}} \begin{cases} 1/a_0^2 & a_0^2 \ll 1 \\ a_0/(3\pi) & a_0^2 \gg 1. \end{cases} \tag{18}$$

The dephasing limit is reached when electrons have travelled half a plasma wavelength (in the frame of the wake) and is given by

$$L_{\mathrm{deph}} \sim \frac{n_{\mathrm{c}}}{n_{\mathrm{e}}} \lambda_{\mathrm{p}} \begin{cases} 1 & a_0^2 \ll 1 \\ 2a_0^2/\pi & a_0^2 \gg 1. \end{cases} \tag{19}$$

Hence, the maximum energy gain is limited by the dephasing length at low intensities but by the depletion length at high intensities and may be estimated together with the maximum electric field E_{p} to

$$\gamma_{\mathrm{max}} \sim \sqrt{2} \frac{n_{\mathrm{c}}}{n_{\mathrm{e}}} \begin{cases} \pi a_0 & a_0^2 \ll 1 \\ a_0^2/3 & a_0^2 \gg 1. \end{cases} \tag{20}$$

3.1.5 Example

In order to get a feeling of the influence of the different parameters, let us consider the following example. A Ti:Sapphire laser system shall be used for electron acceleration. The wavelength is $\lambda_{\mathrm{L}} = 800$ nm and the pulse duration $\tau_{\mathrm{L}} = 100$ fs. The laser pulse energy may be chosen freely as well as the focusing optic.

1. Given by Equation (5), the critical density is $n_{\mathrm{c}} \approx 1.7 \cdot 10^{21}$ cm^{-3}, and from Eq. (14), the electron density required for resonant plasma wave excitation is $n_{\mathrm{e}} \approx 3.1 \cdot 10^{17}$ cm^{-3}. The ratio is $n_{\mathrm{c}}/n_{\mathrm{e}} \approx 5 \cdot 10^3$. The density corresponds to a plasma period of $\lambda_{\mathrm{p}} \approx 60$ μm and the characteristic field strength is $E_{\mathrm{p}} \approx 50$ GV/m.
2. The wave-breaking limit may be calculated from Eq. (16) to $E_{\mathrm{wb}} \approx 600$ GV/m. This gives via Eq. (17) a minimum intensity of $I_{\mathrm{L}} \gtrsim 6 \cdot 10^{20}$ W/cm^2 ($a_0 \gtrsim 16.7$) in order to achieve wave-breaking and self-trapping of electrons.
3. At those intensities ($a_0 \gg 1$), the acceleration length is limited by the depletion length which is of the order of 50 cm. The maximum electron energy is then 300 GeV.

The question now becomes: How can those conditions be achieved? First, the laser must retain its intensity over the whole length. Matching the Rayleigh length $z_{\mathrm{R}} = \pi w_{\mathrm{L}}^2/\lambda_{\mathrm{L}}$ to the depletion length yields a waist of $w_{\mathrm{L}} \sim 400$ μm. This determines the focal spot size A_{foc}. Now, the pulse energy can be calculated, ending up at $W_{\mathrm{L}} > 250$ kJ — a value completely out of range for 100 fs lasers.

Assuming more realistic laser parameters, say $W_L \lesssim 10$ J, one would have to focus down to $w_L \sim 2 \, \mu$m in order to reach the wave-breaking limit. In that case, the acceleration length would be limited by the Rayleigh length which is $z_R \sim 20 \, \mu$m, leading to a maximum electron energy of 10 MeV.

Considering now nonlinear effects, the self-focusing limit leads for the given conditions to a minimum laser power of $P_L \approx 90$ TW which corresponds to a laser pulse energy of $W_L \gtrsim 9$ J. This is still at the upper limit of common pulse energies for 100 fs laser systems. However, if the density is increased, the self-focusing threshold can be lowered and the overall experimental constraints can be loosened significantly. This is the route pursued by the SM-LWFA regime.

3.2 Variants of LWFA
3.2.1 Self-modulated laser wakefield acceleration

In the self-modulated LWFA regime (SM-LWFA), a combination of laser pulse length and plasma density is considered where the pulse is too long to hold condition (14). In this case, the laser pulse still excites a plasma wave by its ponderomotive force, but not as strong as in the resonant case of LWFA. However, the long laser pulse overlaps with the excited wave which represents a periodic density perturbation co-moving with the laser pulse. This density modulation affects the laser pulse. Parts of the laser pulse at positions with reduced electron density propagate faster than parts at positions with increased density, cf. Eqs. (2) and (6). This leads to bunching of the laser pulse, the laser pulse envelope becomes modulated with a periodicity of the plasma wavelength λ_p. As this modulation leads to locally higher intensities, the generation of the plasma wave is enhanced. The density modulation grows, which in turn amplifies the laser pulse modulation. Thus, the pulse splits into pulselets, each separated by the plasma wavelength and now fulfilling the LWFA condition. We see that thereby the LWFA regime can be initiated at significantly less strict conditions than proposed by Eq. (14). In general it is necessary that the pulse power suffices for self-focusing, which in turn can be enabled by high plasma densities.

Let's re-consider the example for the LWFA regime with the following parameters: Again, a Ti:Sapphire laser system shall be used with the same pulse duration of $\tau_L = 100$ fs. However, we choose a density of $n_e = 6 \cdot 10^{18}$ cm^{-3}.

1. Now, the ratio is $n_c/n_e \approx 280$ so that the plasma period is reduced to $\lambda_p \approx 15 \, \mu$m and the characteristic field strength is increased to $E_p \approx 240$ GV/m.
2. The wave-breaking limit is also increased to $E_{wb} \gtrsim 1$ TV/m. However, from Eq. (17) follows a reduced minimum intensity of $I_L \gtrsim 1.5 \cdot 10^{20}$ W/cm^2 ($a_0 \approx 8$) to achieve wave-breaking and self-trapping of electrons.
3. Furthermore, the power threshold for self-focusing is reduced to 5 TW. Hence, laser pulse energies above 500 mJ will lead to self-focusing which overcomes the limitation of acceleration length by the Rayleigh length.
4. If the threshold for self-focusing is passed, also other nonlinearities become effective, making an analytical description difficult. Under self-focusing, the laser diameter is approximately the plasma wavelength—which can be altered further during the interaction. In addition, self-modulation and related effects can lead to effective shortening of the pulse which increases the power. Hence, a 10 J laser pulse will likely reach the wave-breaking limit and could produce 4 GeV electron beams.

As we can see, the SM-LWFA regime is easier to implement than the LWFA regime and may produce higher electron energies for a given laser system (Modena et al., 1995; Esarey et al., 1996). For a predefined pulse duration, a plasma of higher density may be used with a less energetic laser pulse focused more tightly. The interaction length is prolonged by the laser pulse itself via self-focusing, higher longitudinal electric fields are present for acceleration and the intensity threshold is reduced.

Note that if injection shall be accomplished via wave-breaking, there is no possibility to avoid powers and intensities above the threshold for the occurrence of plasma instabilities. Hence, some of the instabilities like self-focusing will always occur, even for the LWFA regime — the transition between the regimes is smooth. However, in the SM-LWFA regime the nonlinear interaction is inteded which makes the whole acceleration process difficult to control. Mostly, exponential electron spectra are obtained due to plasma heating from various instabilities and altered injection conditions for hot plasmas.

3.2.2 The bubble regime

The bubble regime was discovered via computer simulations (Pukhov & Meyer-ter-Vehn, 2002). The simulations include 3D-effects of the plasma wave formation like a tightly focused laser pulse or large transverse oscillations of the electrons but also the mutual interaction between plasma and laser. This regime uses intense ($a_0 > 1$) and very short ($\tau_L <$ 10 fs) laser pulses which propagate through relatively dense plasma ($n_e \sim 10^{19}\,\text{cm}^{-3}$). The simulations show the formation of a bubble-like cavity behind the laser pulse, formed by the transverse deflection of electrons due to the ponderomotive force. This bubble exhibits strong electric fields pointing toward the bubble's centre. Electrons are injected at the rear side of the bubble (wave-breaking) and gather at a small region inside. This can lead to a partial compensation of the electric fields and stop further electron injection (beam loading). The resulting electron beam has, due to this localization, an ultra-short pulse duration, a narrowband energy spectrum and is well-collimated.

From numerous simulations, covering a wide interaction parameter range, simple analytic expressions for the electron bunch properties were derived (Gordienko & Pukhov, 2005). The maximum electron energy is determined by

$$\gamma_{\max} \approx 0.65 \sqrt{\frac{P}{P_{\text{rel}}}} \frac{c \tau_{\text{L}}}{\lambda_{\text{L}}}. \tag{21}$$

Here, $P_{\text{rel}} \approx 8.7$ GW is the relativistic power unit. The number of electrons in the bunch is

$$N \approx 0.28 \frac{\lambda_{\text{L}}}{r_{\text{e}}} \sqrt{\frac{P}{P_{\text{rel}}}}, \tag{22}$$

where $r_{\text{e}} = e_0^2 / (4\pi\varepsilon_0 m_{\text{e}} c^2) \approx 2.8$ fm is the classical electron radius. For laser parameters as discussed in the examples above and now with only 500 mJ of pulse energy ($P = 5$ TW), the maximum electron energy is 300 MeV and the bunch charge 300 pC.

3.3 Experimental studies of laser-electron acceleration
3.3.1 Setup of the laser-driven electron accelerator

A simple but robust and reliable setup for laser-electron acceleration deploys a pulsed gas nozzle in order to generate a *gas jet*, see Fig. 4. The emitted gas density profile changes on

the order of microseconds and can therefore be considered constant during the interaction. The gas is ionized by the leading edge of the laser pulse. Helium is used in order to warrant inert chemical conditions and a fully ionized plasma when the pulse peak arrives. The fraction of laser energy consumed for ionization is negligible. Thus, the high-intensity part of the pulse always interacts with a fully ionized plasma.
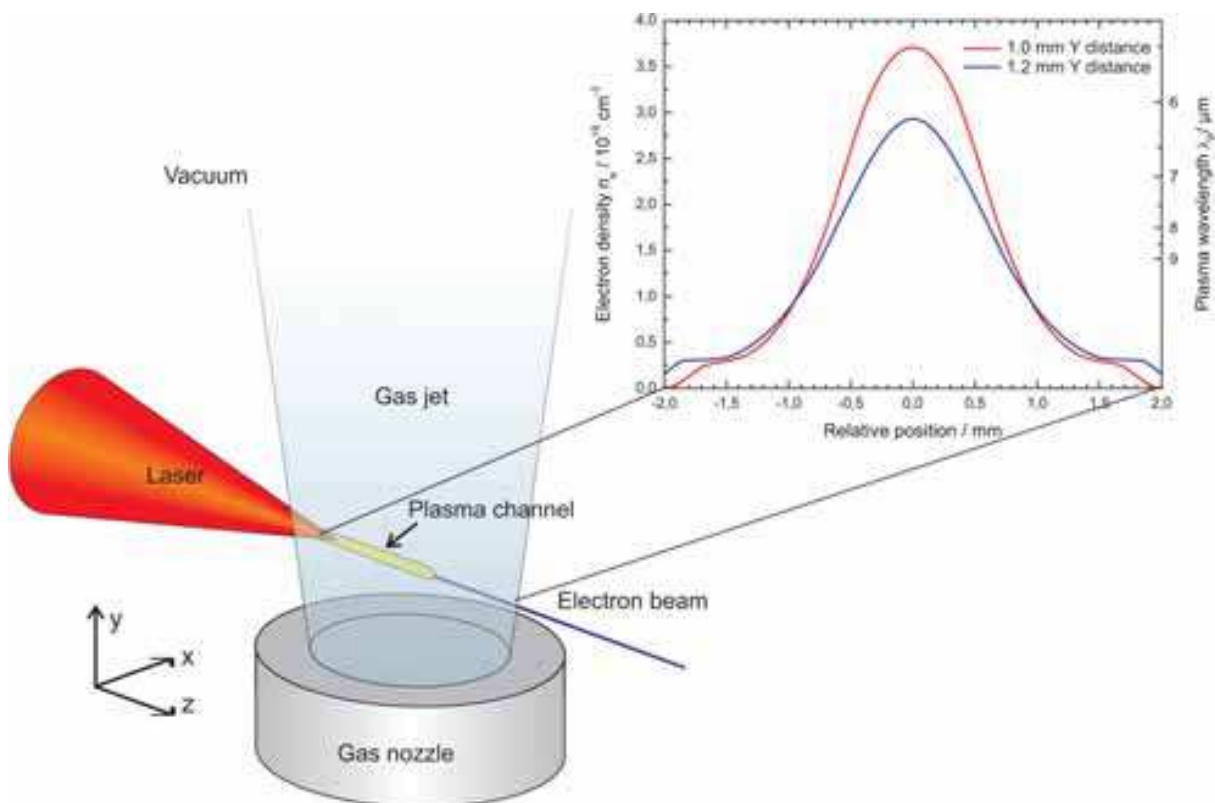

Fig. 4. Schematic of the setup for a laser-driven electron accelerator. An intense laser pulse is focused into a gas jet. Along the laser's path, the gas is ionized. Due to the interaction between laser and plasma at relativistic intensities, the laser pulse propagates in a self-formed channel. In the channel, the laser pulse generates strong plasma waves, wherein electrons are accelerated. All interactions depend strongly on the initial gas density profile, which may be controlled by different nozzle designs. The inset shows typical electron density profiles along the channel for two different vertical distances above the nozzle orifice.

The *electron density profile* along the laser's path therefore depends not on the intensity but on various other parameters: the nozzle orifice shape, the gas flow velocity, the backing pressure, the nozzle opening time and opening duration and, most importantly, the relative position of the laser focus. All these parameters allow for subtle fine tuning of the plasma parameters which turns out to be crucial for a well-controlled laser-driven electron acceleration.

In the here-described experiments, nozzles were used generating gas jets with cylindrical symmetry. The radial density profile has a Gaussian shape and the peak of the density decreases with increasing distance from the orifice. The inset of Figure 4 shows typical electron density profiles for the presented experiments, measured by interferometry of the gas distribution where full ionization of the helium gas was assumed. The nozzle was

cylindrical, had 1.2mm inner diameter, 50 bar backing pressure, 700 μs opening time and a delay between opening and laser incidence of 850 μs.

For these conditions we can estimate which regime of electron acceleration can be obtained. The plasma wavelength changes along the laser propagation and is in the range of λ_p = 6–20 μm (see Fig. 4). The total pulse energy on target is typically ~ 500 mJ and the pulse duration is 85 fs. The focal spot size (FWHM) is about A_{foc} ~ 100 μm². The spot average laser power is $P_{FWHM} \approx 2$ TW and the intensity on the order of I_{FWHM} ~ 10^{18} W/cm². We see that i) the intensity is just at the relativistic limit, ii) the pulse length is too long for resonant excitation (the densities are too high) and that iii) the power suffices for self-focusing in those quite high plasma densities. Thus, direct access to the LWFA regime is not possible, but self-focusing and self-modulation will take place. Earlier experiments with the same laser and subsequent simulations have shown (Hidding et al., 2006) that the mechanism of self-modulation can even lead to the bubble regime. Following the example in Sec. 3.2.2, we can expect collimated electron beams with energies up to hundreds of MeV.

3.3.2 Plasma imaging

The use of gas nozzles has the advantage of unobstructed access to the interaction region. This free access can be exploited by the experimentalist to image the plasma and the channel onto a camera, to image the self-emission from the channel onto a spectrometer, or to deploy short backlighting probe pulses (typically fractions of the main laser pulse) for time-resolved studies. Those *probing techniques* can be shadowgraphy, interferometry or polarimetry and can either use short pulses in a multi-shot scanning regime or chirped pulses for single-shot measurements.
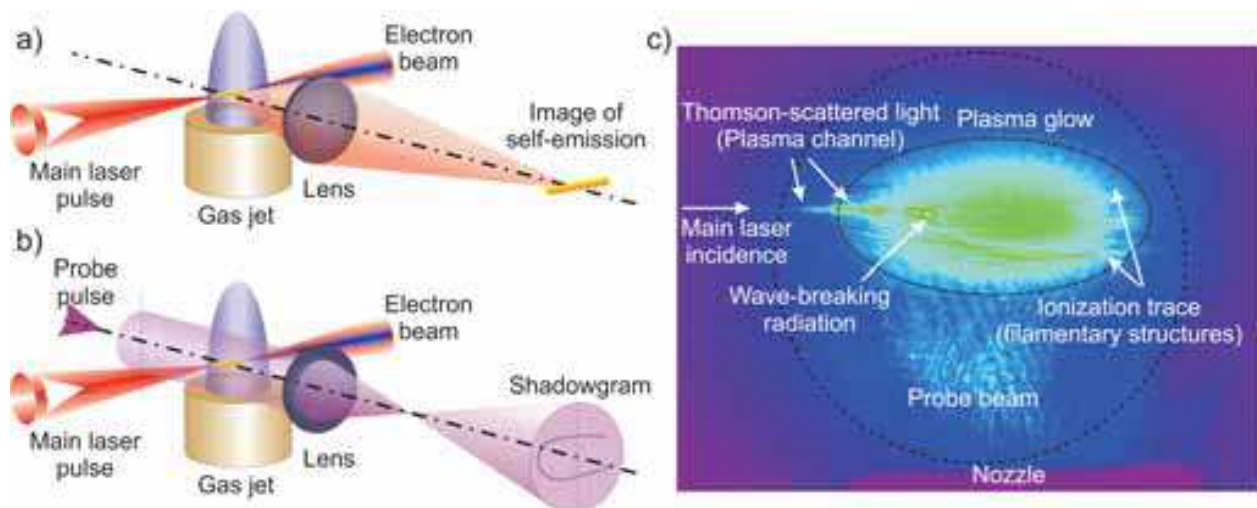

Fig. 5. Setups for imaging of the plasma. Fig. (a) shows mere imaging of the self-emitted light, Fig. (b) depicts imaging of the interaction region with a backlighting probe pulse. Fig. (c) is an image of the interaction region in pseudo-colour representation. This image was taken during setup of the gas nozzle with low plasma density (~ 10^{18} cm⁻³) and with a bandpass filter at $2\omega_L$ (400 nm ± 5 nm). The probe beam (its transverse profile is indicated by the black circle) was activated in order to see the nozzle via its shadow. The laser is incident from the left. The relativistic channel can be observed because of nonlinear Thomson-scattered light. The ionization of the gas is visible from shadowgraphy as approximately horizontal streaks. In the centre of the gas jet (above the nozzle centre), plasma glow is observed.

Figure 5 shows exemplary setups for imaging of the plasma channel (a) and (b) probing of the interaction region with a second, synchronized, much weaker ultra-short laser pulse. The main difference between both is basically whether or not the probe pulse is activated, which can be accomplished with a simple shutter. Experimentally, of course, one has to take care of attenuation with neutral density filters, selection or suppression of wavelengths with interference filters or dispersion of the imaging lens.

Figure 5 (c) shows an exemplary image of the interaction region in pseudo-colour representation. The main laser is incident from the left. The gas nozzle is visible as a shadow at the bottom. The laser pulse undergoes self-focusing and forms a relativistic channel. This plasma channel is partially visible from the nonlinear Thomson-scattered light. After a small gap where the channel is not visible, wave-breaking radiation is emitted (Thomas et al., 2007). The large intense region is the plasma glow. The probe beam was attenuated in order to record both the self-emitted light and a shadowgram. The streaky structures are likely to be ionization traces.

3.3.3 Electron beam properties

In order to characterize the produced electron beams, two diagnostics were deployed. The first one is a retractable scintillating screen which can be inserted into the electron beam path. The induced light signal is proportional to the charge density and is recorded by a camera. This screen allows for measurements of spatial properties of the electron beams. The second device is a dipole magnet spectrometer which deflects electrons depending on their energy. For fixed entrance position and angle, the output position of deflected electrons is a measure for their energy. The detection of electrons is again accomplished by a scintillating screen. These diagnostics allow for real-time acquisition of large amounts of data, which in turn allows for thorough statistical analysis.

Beam profiles and stability Figure 6 shows 4 exemplary electron beam profiles obtained with the scintillating screen for nominally identical experimental conditions. As can be seen, there can be shots with well-collimated beams (a), shots with hardly any electrons (b), fairly collimated and/or multiple beams (c) or rather uncollimated beams (d). For our experimental conditions, this is a typical behaviour for this type of laser-electron accelerator. Slight shot-to-shot fluctuations of the laser beam profile, energy and wavefront may occur and the gas jet exhibits a turbulent flow which means that for consecutive shots there are always small changes of the density profile. Furthermore, the whole acceleration relies on nonlinear interaction: self-focusing, self-modulation, nonlinear plasma wave formation and wave-breaking. The combination of all these factors leads to considerable shot-to-shot fluctuations of the electron beams.

Dependence on the gas jet position The occurrence of well-collimated beams like the one shown in Fig. 6 (a) depends strongly on the interaction conditions which can be easily varied by the gas nozzle position. Basically, the laser can hit the gas jet at any position (x, y, z), whereas typically an axis going through the centre of symmetry of the gas jet is chosen for the laser incidence, i.e. $(x = 0, y, z)$, which corresponds to a radial crossing of the laser through the gas jet. Then, scans in the z-direction are carried out for certain heights y. The vertical distance can be measured from shadowgrams where the nozzle is visible. The condition $x = 0$ is usually set via the brightest emission of Thomson-scattered light. The distance in laser propagation direction can only be determined with help of a separate experiment via a Hartmann aperture in the main beam. The accuracy of all those methods is about 50 μm.
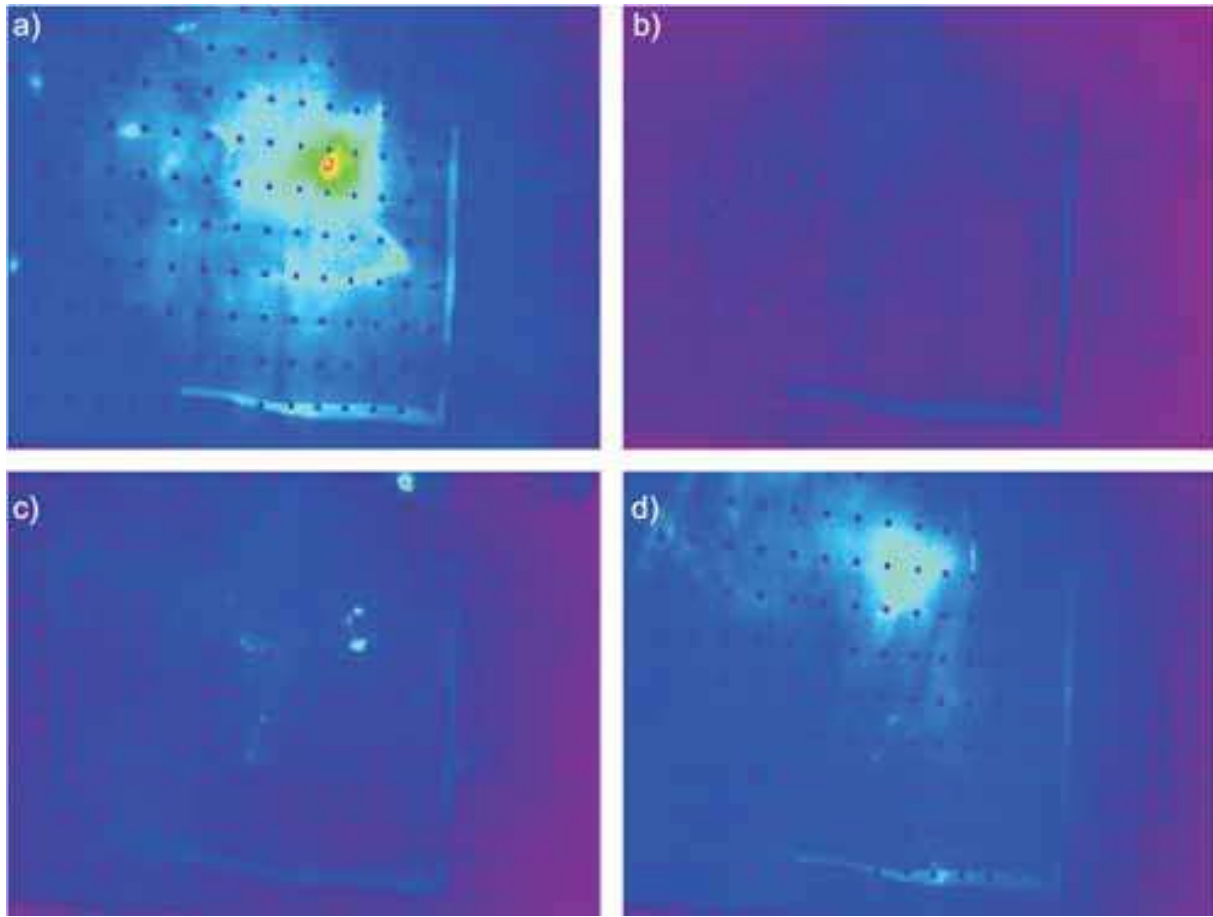
Fig. 6. Example sequence of electron beam profiles in pseudo-colour representation, recorded 30 cm behind the gas jet. The point grid has a 5 mm spacing in the vertical direction.

A typical result of such scan is shown in Figure 7. Positive values for the z-position indicate that the laser focus (in vacuum) is behind the gas jet centre. At each position, 10 to 20 shots were carried out and the aiming screen images were averaged. From such an averaged image, the sum brightness (sum over all pixel values) is a measure for the average charge per shot. From the averaged image itself, the mean direction of electrons can be inferred. The average charge as function of gas jet position is plotted in Figure 7 (a). Furthermore, from the single images of the aiming screen, the relative frequency of well-collimated beams can be counted and plotted in the same manner, see Figure 7 (b). Then, through systematic scanning in z and y, the optimum position can be found, either for high average charge or frequent occurrence of well-collimated beams or both.

Generally, a too small vertical distance y between laser incidence and gas nozzle (and therefore a high peak plasma density, cf. Fig 4) leads to a higher charge but less frequently collimated beams. Instead, electrons are distributed in a considerably large cone of about 30 mrad full opening angle. This is reasonable since at too high gas densities, the self-modulation becomes stronger and the regime of DLA is entered which is not desired for collimated and potentially monoenergetic electron bunches. In the longitudinal direction, an optimum is found slightly behind the point where the vacuum focus coincides with the gas jet centre. That means that a relatively long path in an increasing density profile is required for self-modulation and self-focusing.
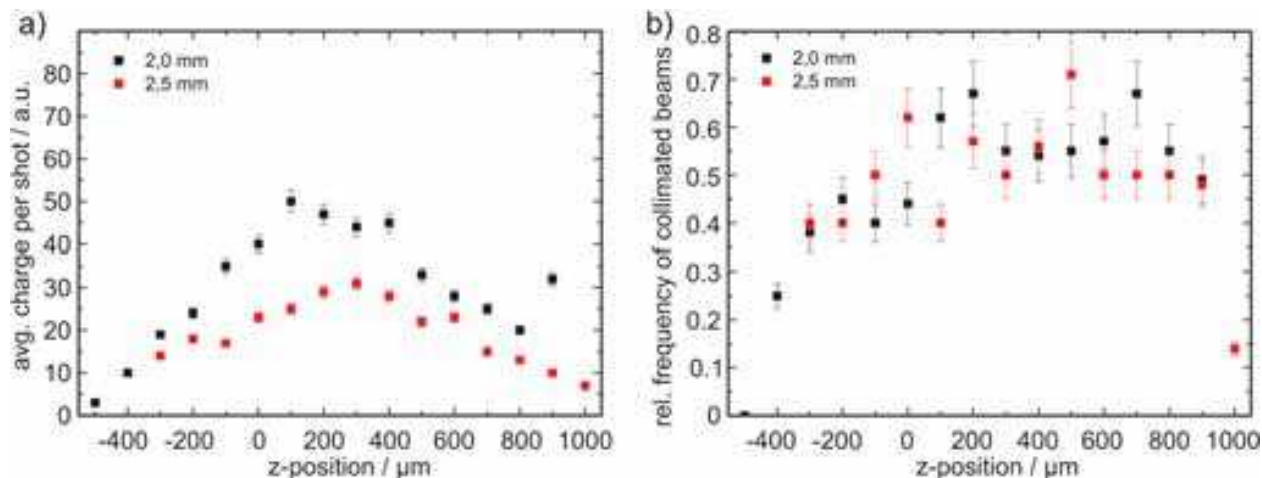
Fig. 7. Optimization of the interaction geometry. Shown are the average charge per shot (a) and the relative frequency for well-collimated beams (b) as a function of the longitudinal position z for two vertical distances y between nozzle and laser focus (black and red squares). Note that the difference of the vertical distance in contrast to Fig. 4 is due to a different nozzle.

Spatial characteristics of well-collimated beams Well-collimated beams may be also characterized in terms of size and spatial (angular) distribution. This is shown in Figure 8 for a nozzle position optimized for frequent occurrence of well-collimated beams. As can be seen, the beams propagate in average close to the on-axis direction but with a mean deviation of about 40 mrad. This is considerably high for applications but is sufficient for studies and can be reduced by other experimental approaches (see Sec. 3.4). The divergence of electron beams can be as low as 2 mrad. In comparison with results from other groups, this is remarkably low for gas jet targets and is suited for applications.
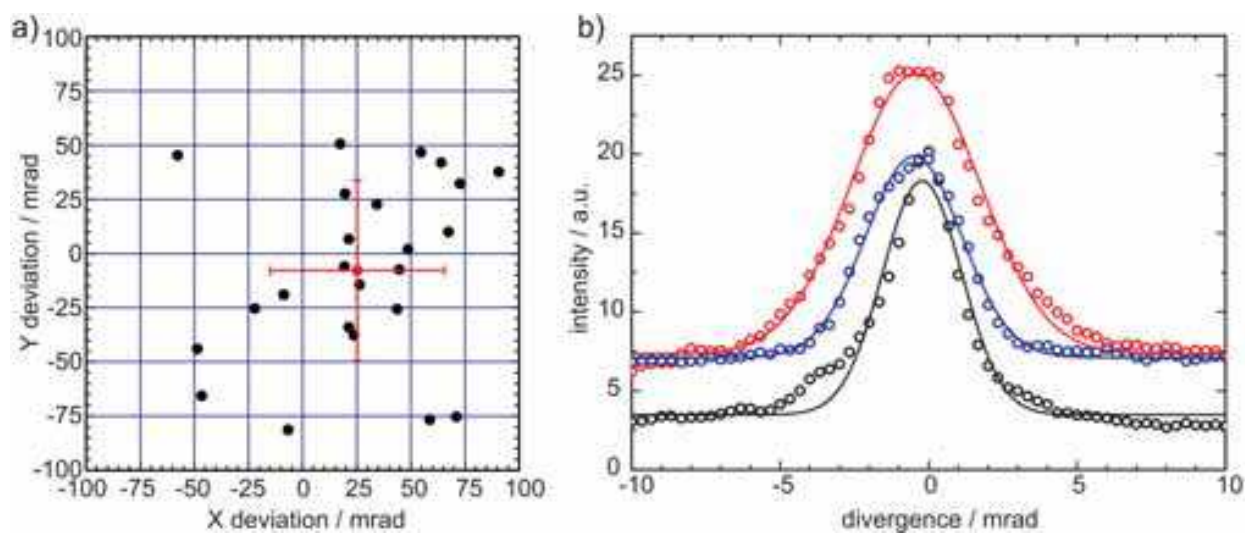

Fig. 8. Pointing (a) and divergence (b) of well-collimated electron beams under optimized nozzle conditions. Shown in (a) is the pointing direction with respect to the laser axis. The red cross represents the average position and the standard deviation. For (b), lineouts of the scintillating screen images were taken. The Gaussian fits have widths of 2–4 mrad.

Spectral characteristics Considering the spatial fluctuations of well-collimated beams and the acceptance angle of the electron spectrometer, we expected to rely on the high repetition rate and the fast online diagnostics in order to record sufficient electron spectra for a comprehensive statistical analysis. It turned out that electron spectra were measured much more frequently than expected. This was caused by the fact that also electrons contributing to the cloudy background on the scintillating screens were measured with the spectrometer and showed monoenergetic features which both was not expected.

Figure 9 shows typical electron spectra. Raw images from the scintillating screen of the electron spectrometer are displayed in Fig. (a)–(c). Figure (d) shows the corresponding calibrated spectra. Note that the shadow in the left part of each image is caused by a frame inside the spectrometer, used for calibration. The energy range shown in the spectra corresponds to the part right of the shadow.
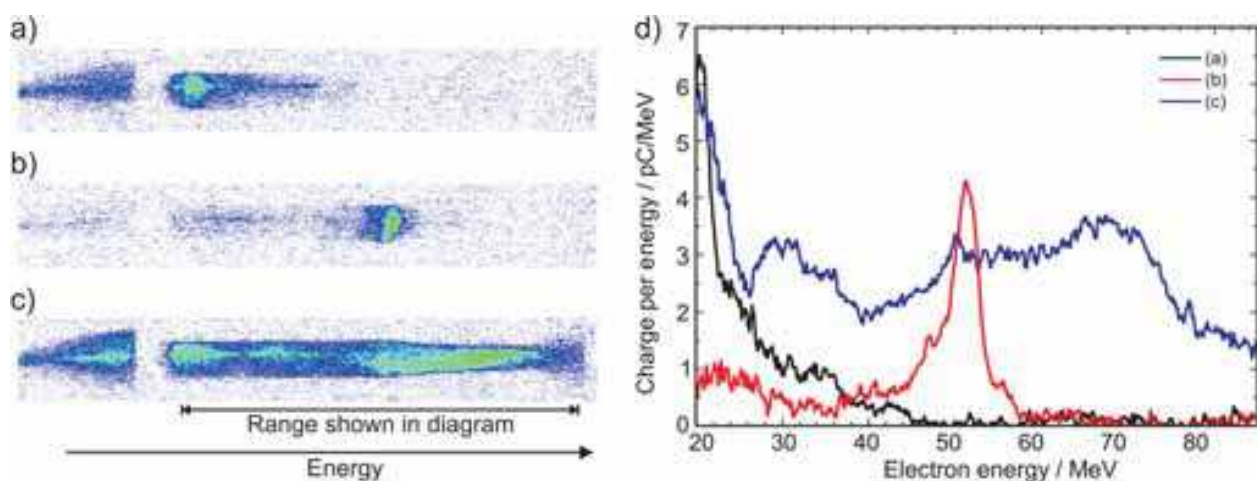

Fig. 9. Typical electron spectra, as raw data from the scintillating screen of the spectrometer (a)-(c) and as calibrated spectra (d). The gap in the left part of each image is caused by a frame inside the electron spectrometer and ranges from 16 MeV to 20 MeV.

Shot (a) shows an exponential spectrum, in this case quite intensive and therefore ranging to comparably high energies. Shot (b) shows a typical monoenergetic spectrum at 50 MeV. The bandwidth shown in the spectrum is about 4 MeV FWHM. Spectrum (c) is very broad which is a rare event. It reaches the high-energy limit of the spectrometer which is at 85 MeV.

Electron spectra can be categorized (similar to electron beam profiles) into exponential, monoenergetic, "empty" and irregular (all other) spectra. Out of a typical set of 200 laser shots at an optimized gas nozzle position, only 29 shots produced almost no electrons detectable by the spectrometer, either caused by insufficient charge at all or collimated beams propagating off axis. Other 33 shots showed exponential spectra which usually extended to 20–25 MeV. 47 shots were dominated by monoenergetic features. The remaining 91 shots could not be designated unambiguously into one of those categories. Hence, about every fourth shot is monoenergetic, however, charge and peak energy are fluctuating.

The monoenergetic spectra were analysed further. Figure 10 shows the distribution of charge (a) and energy (b) of 47 shots producing monoenergetic spectra. Figure 10 (a) shows a broad plateau up to 45 MeV for the energy distribution. The charge distribution, Fig. 10 (b), shows also a roughly constant plateau up to 40 pC. Higher charges of within a monoenergetic peak are rare. Note that a plot of peak charge versus peak energy revealed no correlation between both quantities.
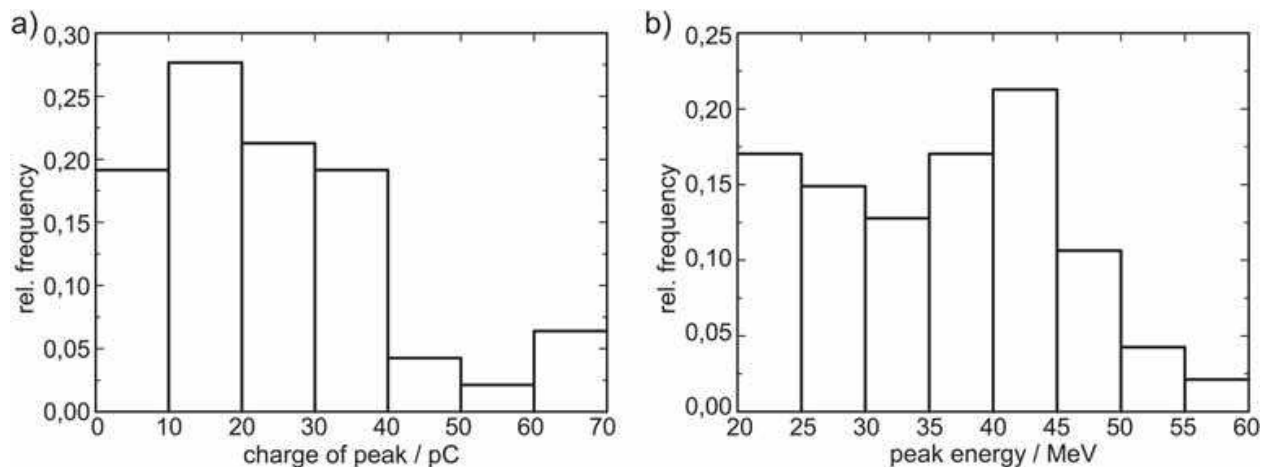
Fig. 10. Histograms for monoenergetic electron spectra, showing the frequency distributions of charge (a) and energy (b).

3.4 Ways to improved electron acceleration

The here-described laser-plasma accelerator relies on nonlinear interaction and feedback between laser pulse and plasma wave. The laser pulse a) guides itself (self-focusing), is meanwhile b) shortened by the plasma (self-modulation) and can then drive a plasma wave so strongly that c) injection via wave-breaking occurs. The setup is relatively simple and robust and allows for various investigations of the interaction region. However, the produced electron beams are subject to non-negligible fluctuations in terms of pointing and spectral parameters, which is largely due to the afore-mentioned nonlinear interactions.

Other groups in the field of laser particle acceleration proposed and demonstrated different experimental setups which produce electron beams more stably. A key feature of all these setups is that more powerful laser systems are used (more pulse energy and/or shorter pulses) and the laser pulse and its interaction with the plasma are not solely used for all the 3 steps a)–c). In particular, there is a general trend towards quasi-linear regimes (not being very reliant on nonlinearities) and to dedicated processes or means (even physically separated sections or stages) for the steps a)–c). A few but important examples shall be described in the following.

3.4.1 Shorter laser pulses

Many experiments have been carried out at laser facilities with shorter laser pulses, typically $\tau_L \sim 30$ fs, where electron energies of a few 100 MeV were obtained from gas jet targets (Mangles et al., 2004; Malka et al., 2005). Being initially shorter, the pulses have to undergo less nonlinear self-forming processes which smooths the interact. Moreover, those laser systems produce comparable pulse energies of ~ 1 J, but due to the shorter pulse the power is higher. Consequently, longer focal lengths can be used which was found to be beneficial for stable electron beam generation. Recently, electron beams were produced using a sub-10-fs laser system which directly accessed the bubble regime, i.e. without self-modulation (Schmid et al., 2009).

3.4.2 Guiding

In addition to self-focusing, external means can be used to counteract diffraction and thereby prolong the interaction length. Over the last few years, the use of capillary discharge

waveguides was successfully implemented by several groups. Electron beams of up to 1 GeV kinetic energy within a beam of less than 2 mrad divergence and with negligible pointing jitter were obtained due to longer acceleration lengths (Leemans et al., 2006; Karsch et al., 2007; Rowlands-Rees et al., 2008), which is considered as a major breakthrough in laser-driven electron acceleration.

This type of plasma waveguide relies on thermal equilibrium of a gas discharge in a narrow capillary. The discharge current ionizes and heats the plasma which is cooled at the walls. Thereby, the temperature in the centre rises, the plasma density becomes thinner and a focusing density profile is formed. However, this approach increases the experimental complexity. In addition it should be noted that any external guiding structure is just an additional or assisting feature since a relativistically intense laser pulse always exhibits self-focusing.

3.4.3 Homogeneous plasma

The above-mentioned guiding experiments use a capillary with two gas injection slots close to the entrance and exit of the capillary. In recent experiments, similar capillaries were used as gas cell (Osterhoff et al., 2008), i.e. without discharge and therefore without external guiding. It was shown that electron beams can be produced very stably with 200 MeV peak energy, 2 mrad divergence and 1.4 mrad pointing jitter. This result is attributed to a very smooth plasma density profile. After filling, there is no gas flow between the gas injection slots. In contrast, gas jets always exhibit a gas flow where turbulences may be present. Those weak density fluctuations may lead, regarding the nonlinear nature of the underlying laser-plasma interaction, to less stable results and considerable shot-to-shot fluctuations. This may also explain the good results of capillary-guiding experiments.

3.4.4 Advanced injection techniques

It has been described before (cf. Sec. 3.1.3) that the electron acceleration relies on the injection of electrons into the strongly excited plasma. In our presented experiments, this was achieved by driving the wave to the nonlinear regime of wave-breaking which is accompanied by strong fluctuations. In contrast, if the injection of electrons is triggered externally, there is no need to drive the plasma wave so strongly that it reaches the nonlinear regime and the wave-breaking limit.

One way is beatwave injection (Faure et al., 2006). In addition to a strong laser pulse driving a non-breaking plasma wave, a weak counter-propagating laser pulse is used which interferes with the strong one inside the plasma. A standing wave is formed at the edge of the intense pulse. At this region, electrons oscillate relativistically in laser propagation direction. A fraction of electrons obtains sufficient energy in order to co-propagate with the plasma wave driven by the strong laser pulse. It was shown that monoenergetic electron beams can be generated very reliably. The energy can be chosen by the delay between and therefore by the overlap position of the two pulses. The longer the distance from the laser overlap to the end of the plasma, the higher the energy. Furthermore, by changing the amplitude of the standing wave, charge and energy spread of the electron bunch can be controlled.

Another possibility is ionization by the main pulse. If the gas is not fully ionized before the main pulse arrives, the residual ionization is accomplished by the pulse peak. Evidence was found that this late ionization leads to more stable electron beams. In one experiment,

capillary discharge waveguides were used. It was observed that the discharge did not fully ionize the gas and that ionization by the laser assisted the injection process (Rowlands-Rees et al., 2008). In very recent experiments, spurious amounts of gases like Nitrogen or Neon were added to the Helium of the gas jet. Hence, those atoms or partially ionized ions become ionized by the main pulse. Simulations show that tunnel ionization might be responsible. However, the observations are not yet fully explained and more work is under way.

A third route towards more controlled injection is the use of an electron density downramp (Geddes et al., 2008). If the plasma density decreases along the laser propagation direction, the plasma wavelength increases. This causes the plasma wave fronts to fall further behind as the laser propagates and effectively decreases the wake velocity. Hence, electrons require lower velocities to catch the wake and thereby the injection threshold is lowered. It was shown that with high reproducibility, low energy electrons (~ 0.8 MeV) with very low absolute energy spread (~ 0.2 MeV) can be produced, additionally with low transverse spread, good beam pointing and high charge (~ 1 nC). Very recently, this was combined with a second interaction stage for electron acceleration. The result is that the low-energy electrons are accelerated to much higher energies whereas the absolute energy spread remains small, yielding a very small relative energy spread. This represents a remarkable step towards future applications, allowing for small energy spread combined with high electron energies and stable beams with a single laser pulse focused into a single device.

4. Laser-based ion acceleration

In this section we will describe the physical concept of ion acceleration using high-intensity laser systems. In contrast to electrons, ions of mass $m_i = A \cdot 1836 \cdot m_e$ are hardly affected directly by the laser pulse. Hence, with today's laser intensities there is no effective energy transfer possible. Therefore, laser-based ion acceleration takes place as a secondary effect and is typically realized with thin foil targets of a few micrometer thickness, whereas various mechanisms have been identified as the source of the energetic ion beams (Snavely et al., 2000; Sentoku et al., 2003; Fuchs et al., 2005). The most widely investigated and used mechanism is *Target Normal Sheath Acceleration* (TNSA), which relies on three steps.

- An energetic, hot electron contribution is created by the interaction of a laser pulse with overdense plasma.
- The electrons propagate into the plasma. Usually, thin metal foils of a few microns thickness are used as target.
- At the target foil rear side, electrons leave the target and form a kind of capacitor. In the electric field arising from this charge separation, atoms from the rear side become ionized and subsequently accelerated. This is the key process of TNSA.

After presenting this standard model for laser-driven ion acceleration, we will extended it for the generation of ion beams with intrinsically narrowband spectra. After that, we will present experimental results of producing narrowband beams. We will show the special experimental setup, explain the necessary steps and discuss the obtained results. Most notably, we performed systematic studies from which we derived a scaling law of proton peak energy as function of the laser pulse energy.

4.1 TNSA – Target normal sheath acceleration of ions

The physical picture of Target Normal Sheath Acceleration of ions is displayed in Fig. 11: An intense laser pulse irradiates the front of a thin solid target. A relativistic electron population

is generated that propagates through the target. If the target is chosen thin enough (i.e. typically a metal foil target of a few μm thickness), the electrons reach the back surface without considerable energy loss. The fastest electrons escape the target which thereby becomes positively charged up. The main part of the population is trapped by the electric field generated as a result of charge separation, forming a *sheath* of hot electrons at the back surface of the target, see Fig. 11 (b). As mentioned in Sec. 2.3, the electron distribution can shield the positive charge of the target only to the order of the Debye length λ_D. The available electric field strength due to this uncompensated positive charge is of the order of 10^{12} V/m. Such field strengths suffice to field-ionize atoms (cf. Sec. 2.2) present at the back surface of the target. Those atoms can be the target foil material itself, layers of contaminants (comprising hydrocarbons and water vapour), or additionally deposited material, which constitute the *ion source*. As soon as ions are generated, they are accelerated according to their charge to mass ratio q/m. Hence, protons as the lightest ion species will be most accelerated. A selection of ion species is in general only possible if the source's chemical composition is controlled, i.e. contaminants are suppressed. As shown in Fig. 11 (c), at a later time the ion front expanded into the laser-driven electron sheath at the target rear side. Since the electric field is oriented perpendicular to the conducting surface of the target, the ions are accelerated in *target normal direction* which lead to the name of Target Normal Sheath Acceleration.
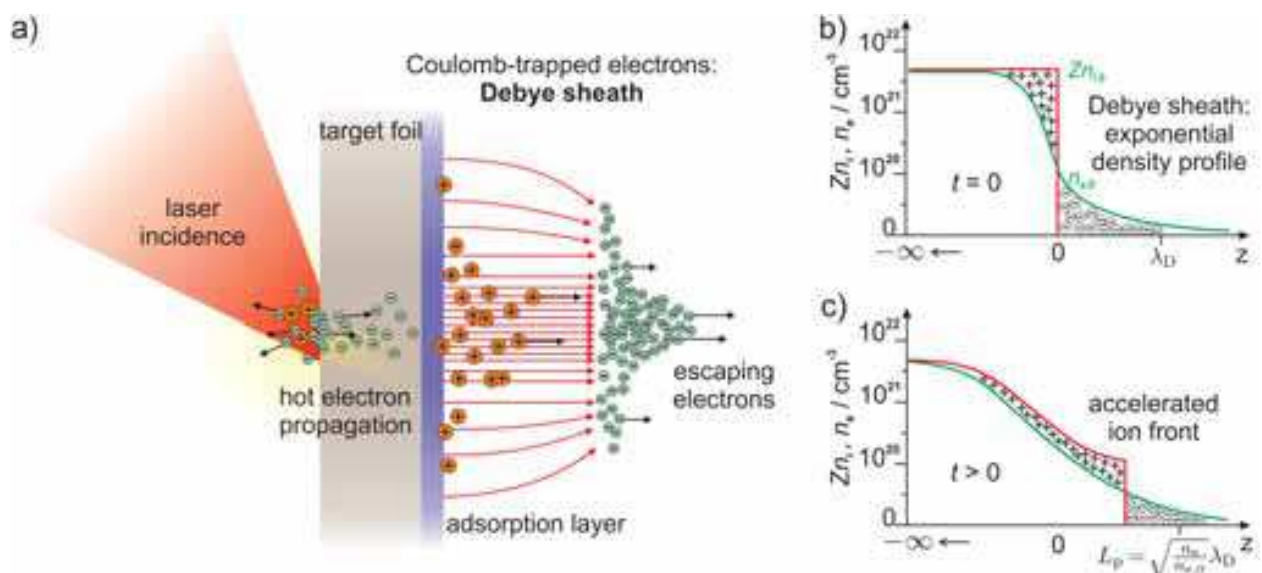

Fig. 11. The schematics of the TNSA process (a) and electron and ion density distribution at the beginning (b) and at a later time (c) of the acceleration. Here, protons are considered as the only ion species present.

4.1.1 Electron transport through the target foil

The total number of electrons produced by the absorption and electron heating processes at the target front side (cf. Sec. 2.7) can be deduced with the help of a simple estimation. As an example, consider a 500 mJ, 100 fs laser pulse, applying an intensity of $2 \cdot 10^{19}$ W/cm^2 ($a_0 \approx 3$) to the target and producing a hot electron population with an energy conversion

efficiency of about 20 % (cf. Sec. 2.7). From the laser's ponderomotive potential, Eq. (12), one can estimate the temperature of the electron population to be 1.1 MeV. Energy conservation leads to the total number of hot electrons of $N_e = 5.7 \cdot 10^{11}$.

This electron bunch, travelling through the target, forms a current of $J = e_0 N_e / \tau_L \sim 1$ MA, a value substantially exceeding the Alfvén limit $J = \beta\gamma \cdot 17$ kA, i.e. the maximum electron current that can propagate freely in vacuum (Alfvén, 1939). However, the propagation of such a hot electron current becomes possible in a conductor due to return currents that compensate the self-induced azimuthal magnetic fields around the relativistic electron forward current. In addition, the background electron density is of the order of the solid density $n_e \approx 10^{23}$ cm^{-3} and consequently much higher than the density of the relativistic electron beam, $n_e < n_c \approx 10^{21}$ cm^{-3}. Hence, the return currents are provided by a cold electron population obtaining just a slow drift. Furthermore, by using a conducting target material, the influence of magnetic field fluctuations or Weibel instabilities can be neglected since free charges are available to provide the necessary return currents. Consequently, a smooth electron beam with Gaussian temporal and spatial shape due to the laser pulse properties will propagate through the target (Honrubia et al., 2005). However, ohmic losses via collisions with the target foil atoms are still present and lead a reduction of the electron temperature at the rear side and a spread-out of the electron bunch.

4.1.2 Analytical model of the sheath field acceleration

The TNSA process can be analytically modelled as an isothermal plasma expansion into vacuum (Mora, 2003), considering only the target normal direction and disregarding transverse dependencies (1D model). This expansion is depicted in Fig. 11 (b) and (c). One can derive the maximum ion energy,

$$W_{max} = 2Zk_B T_e \left[\ln\left(\tau + \sqrt{\tau^2 + 1} \right) \right]^2,$$ (23)

as well as the ion spectrum (per surface unit),

$$\frac{dN}{dW} = \frac{Zn_{e,0}t}{\sqrt{2Wm_i}} \exp\left[-\sqrt{\frac{2W}{Zk_B T_e}} \right].$$ (24)

Here, Z is the charge state, $\tau = \omega_{p,i}\, t/\sqrt{2e}$ a normalized time correlated to the acceleration time $t = \tau_{acc}$, $n_{e,0}$ the initial electron density of the hot electron distribution driving the whole ion acceleration process and $\omega_{p,i}$ the plasma frequency (cf. Eq. (2) but with m_i instead of m_e) of the considered ion species.

The acceleration time τ_{acc} as one of the main free parameters has been found to be in good accordance with the following formula:

$$\tau_{acc} = \alpha(\tau_L + 60\,\text{fs}),$$ (25)

with $\alpha = 2.6$ decreasing linearly from 10^{19} W/cm² to the constant value of $\alpha = 1.3$ for $I \geq 3 \times 10^{19}$ W/cm² (Fuchs et al., 2007). Following the example above, Eq. (25) gives an acceleration time of 310 fs.
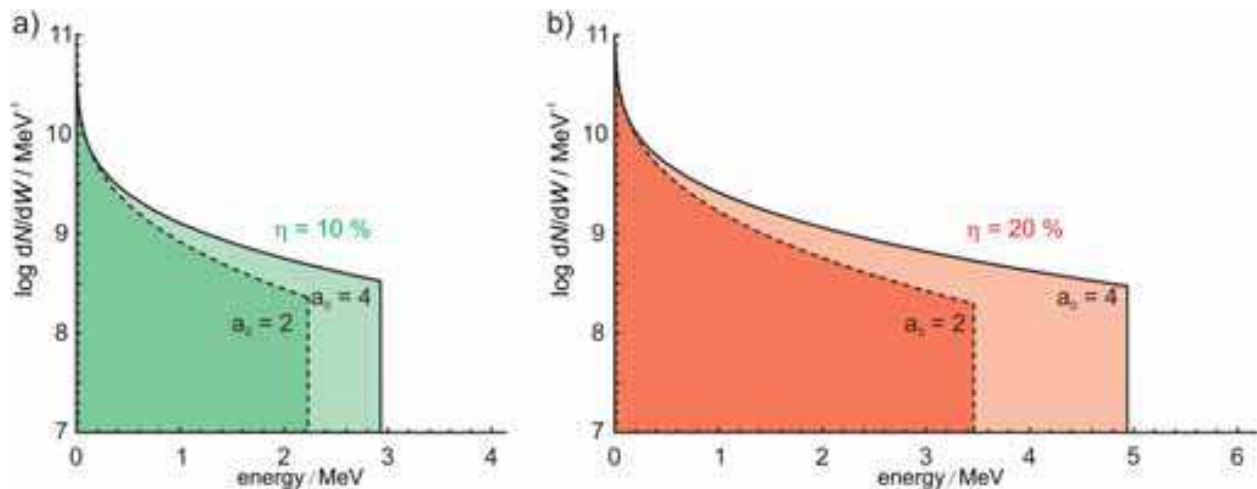
Fig. 12. Proton energy spectra calculated according to Eqs. (23) and (24) for different laser intensities a_0. The green spectra on the left hand side (a) consider a conversion efficiency η of 10 % whereas the red spectra (b) stand for $\eta = 20$ %. Taken from (Jäckel, 2009).

Regarding the second major free parameter of the model, the initial electron density, one may take the above-estimated total electron number (cf. Sec. 4.1.1), the bunch length $c\tau_L$ and needs to consider a spreading of the hot electron beam propagating through the foil, leading to an effective area covered by the electron bunch when it exits the target, $A_{\text{Sheath}} = \pi [r_{\text{eff}} + d_{\text{eff}} \tan(8°)]^2$ (Kaluza et al., 2004), to arrive at the following expression:

$$n_{e,0} = \frac{N_e}{A_{\text{Sheath}} c\tau_L}. \tag{26}$$

Here, a typical divergence of the electron beam inside the target of 8° can be assumed in good accordance with simulations and experiments. The parameters r_{eff} and d_{eff} take into account the incidence angle of the laser pulse onto the target, which is mostly 45°: $d_{\text{eff}} = d_{\text{target}}/\cos(45°)$ and $r_{\text{eff}} = w_L/\cos(45°)$ (Honrubia et al., 2005). Typical values of the initial electron density of the target rear side sheath are of the order of 10^{20} cm^{-3}.

Using τ_{acc} and $n_{e,0}$ and assuming a laser intensity equivalent to $a_0 = 2\text{-}4$, one obtains the proton spectra displayed in Fig. 12. The spectra show a quasi-thermal distribution with a distinct maximum energy. This maximum energy depends on both the absorption efficiency and the laser intensity.

4.1.3 Influence of the target thickness
In order to extend the discussion of the electron transport through the target, the influence of the target foil thickness on the produced ion beams will be introduced in the following. Fig. 13 shows measured proton spectra, produced from Titanium foils of different thicknesses ($d_{\text{target}} = 1 - 20 \mu$m). The number of protons is given per 0.01 MeV energy interval and 1 μsr solid angle of detection and is plotted against the proton energy. The laser parameters are identical to those of the results presented later in Sec. 4.3. We observe quasi-thermal proton spectra with distinct maximum proton energies, as discussed in the previous section. However, we find, now regarding the target thickness, a specific trend: with decreasing foil thickness, we observe an increase of both the total proton number and the maximum proton energy for each spectrum until an optimum value of $d_{\text{target}} = 2 \mu$m.
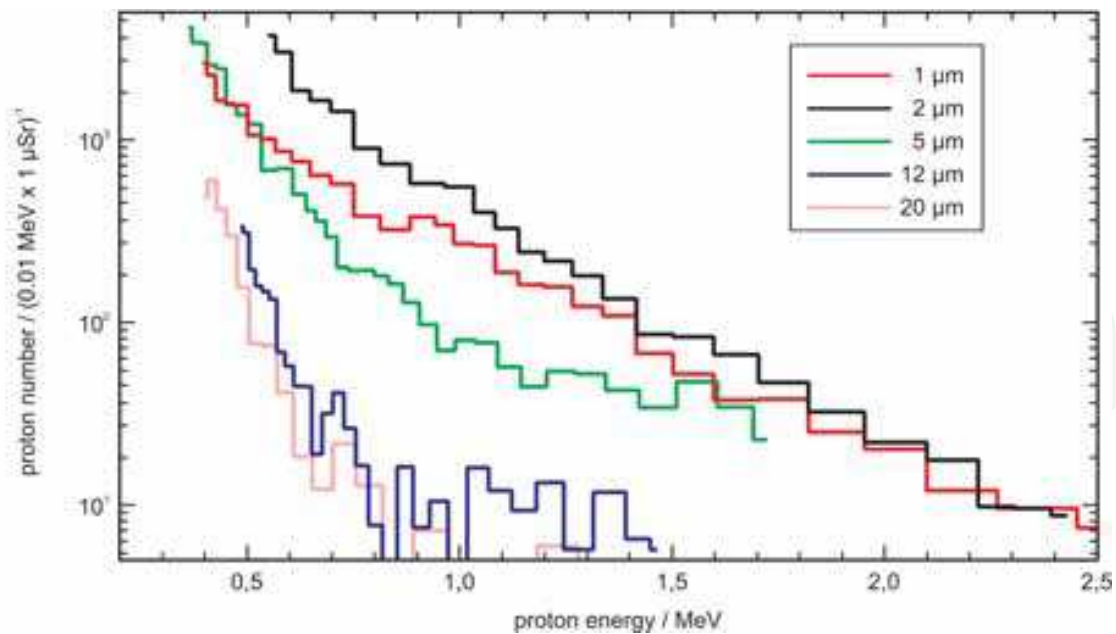
Fig. 13. Proton spectra for different target foil thicknesses.

This characteristic behaviour can be explained as follows. For decreasing foil thickness, the electron transport becomes more effective since the influence of the resistivity decreases for a shorter propagation length through the foil material, and hence the electron temperature remains higher when the electrons reach the target back surface. Furthermore, the electron sheath behind the target foil has a higher electron density since the electron beam is less transversely spread throughout the shorter propagation path, cf. (26). Thus, both parameters which characterise the initial electric field strength, $E_{\mathrm{TNSA}} = \sqrt{2/e \cdot k_{\mathrm{B}} T_{\mathrm{e}} \cdot n_{\mathrm{e}} / \varepsilon_0}$, being responsible for laser ion acceleration, contribute positively and amplify the acceleration process. In principle, this trend can be shifted to ever thinner targets and is only limited by the temporal contrast of the laser pulse. The laser pulse contrast determines the preplasma formation at the target front side, which eventually can break through the target foil if it is very thin. In the present case, the laser pulse conditions dictate an optimum target thickness of $d_{\mathrm{target}} = 2\,\mu$m. A further decrease of the thickness gives only spectra with lower proton number and maximum energy. However, this concept of decreasing target thickness and increasing laser contrast is an important route of today's research on laser ion acceleration, see (Henig et al., 2009) for example.

4.2 Generation of monoenergetic ion beams – Confined TNSA

The proton (or ion) beams produced via TNSA typically show an exponential energy spectrum with a distinct cutoff energy W_{max} of typically a few MeV, which depends strongly on the laser and target parameters, cf. Fig. 13 and (Kaluza et al., 2004). This broad distribution can be explained mainly by two contributions: First, the accelerating electric field decays when reaching into regions of higher charge density. Deeper-sited protons in the source will thus be partially screened from the electric field by their predecessors. Thus, the proton's final energy is determined by its initial longitudinal position. Secondly, the accelerating sheath field typically possesses a bell-shaped symmetry and is inhomogeneous in the transverse direction (which is actually not included in the mathematical model but does not substantially diminish its explanatory power). That means that the maximum

energy a proton can gain is also determined by its radial distance from the laser spot. Protons located in the centre of the field are accelerated the most up to the maximum energy W_{max}, whereas protons outside experience a lower electric field strength and consequently are accelerated to lower energies. As a consequence of both the screening effect and the transverse inhomogeneity of the electric field, the resulting spectrum has a strong correlation to the initial distribution of the protons to be accelerated from the target.

Following this understanding, Esirkepov and Bulanov proposed an acceleration scheme for the generation of monoenergetic beams where all protons are *radially confined* to a "dot" source within the central homogeneous region of the TNSA field (Esirkepov et al., 2002). If the proton source is furthermore sufficiently thin so that screening effects are negligible, all protons experience the same potential and are accelerated to a monoenergetic distribution.

This is depicted in Figure 14 (a). Similar to standard TNSA, an intense laser pulse impinges onto a thin target foil and generates a sheath of hot electrons at the target back side. But now, there is a dot instead of transversely extended layers, constituting a thin, radially confined ion source being located in the central homogeneous field region.

Recent theoretical studies (Robinson & Gibbon, 2007) showed that the limitation of the source thickness is actually not a critical criterion, but that for "thicker" dots, the formation of monoenergetic spectra is supported by *charge separation effects* between two ion species with different charge to mass ratio q/m, e.g. protons and carbon, cf. Fig. 14 (b)–(d). Robinson & Gibbon showed in a detailed study regarding micro-dot acceleration that monoenergetic spectra can in fact be produced from dots of up to micrometer thickness and may even vanish if the source layer is chosen too thin.

So how does the charge separation mechanism work? Consider a confined ion source consisting of two ion species, say protons and C^{4+}. Owed to their different q/m-ratios, the two ion species are accelerated differentially according to $\ddot{z} = q/m \cdot E_z$, and will hence separate at an early stage of the acceleration process. Consequently, two particle distributions with distinct particle fronts will propagate away from the target surface. This situation is shown in Fig. 14 (b): The fast proton front (red) and the slower carbon front (green) each terminate at a sharp z-position, whereas the carbon front overlaps with the low energy part of the proton distribution. Fig. 14 (b) represents a snapshot taken from a 1D-PIC simulation by Alex Robinson (Robinson et al., 2009) for a 1 μm thick target located at $z = 0$, at a laser intensity of $I_L = 10^{20}$ W/cm^2. The total charge density is plotted in Fig. 14 (c). It displays two distinct discontinuities, one at the proton front ($z \approx 6\ \mu$m), and one at the carbon front ($z \approx 4\ \mu$m). Recall that TNSA is driven by charge separation at the solid-vacuum interface, where hot electrons are accelerated across the proton front and trapped to constitute the TNSA sheath field. Obviously, the same holds true for the charge discontinuity at the heavy ion front: The discontinuity represents a boundary where charge neutrality cannot be retained, and passing hot electrons will hence form a second sheath field across the carbon front. This is illustrated in Fig. 14 (d), where the electric field behind the target is plotted. The two strong peaks correspond to two electrostatic shocks resulting from the sheath fields at the proton and heavy ion front, respectively. Between the peaks, there exists a zero-field region ($z \approx 5.5\ \mu$m), at which the proton front sheath field is already screened such that protons, accompanied by a colder electron population, may propagate undisturbed in quasi-neutrality. This zero-field region is where protons accumulate to form a stable monoenergetic bunch. Similar to the TNSA process at the proton front, the light protons from the low energy part of the spectrum are efficiently accelerated across the
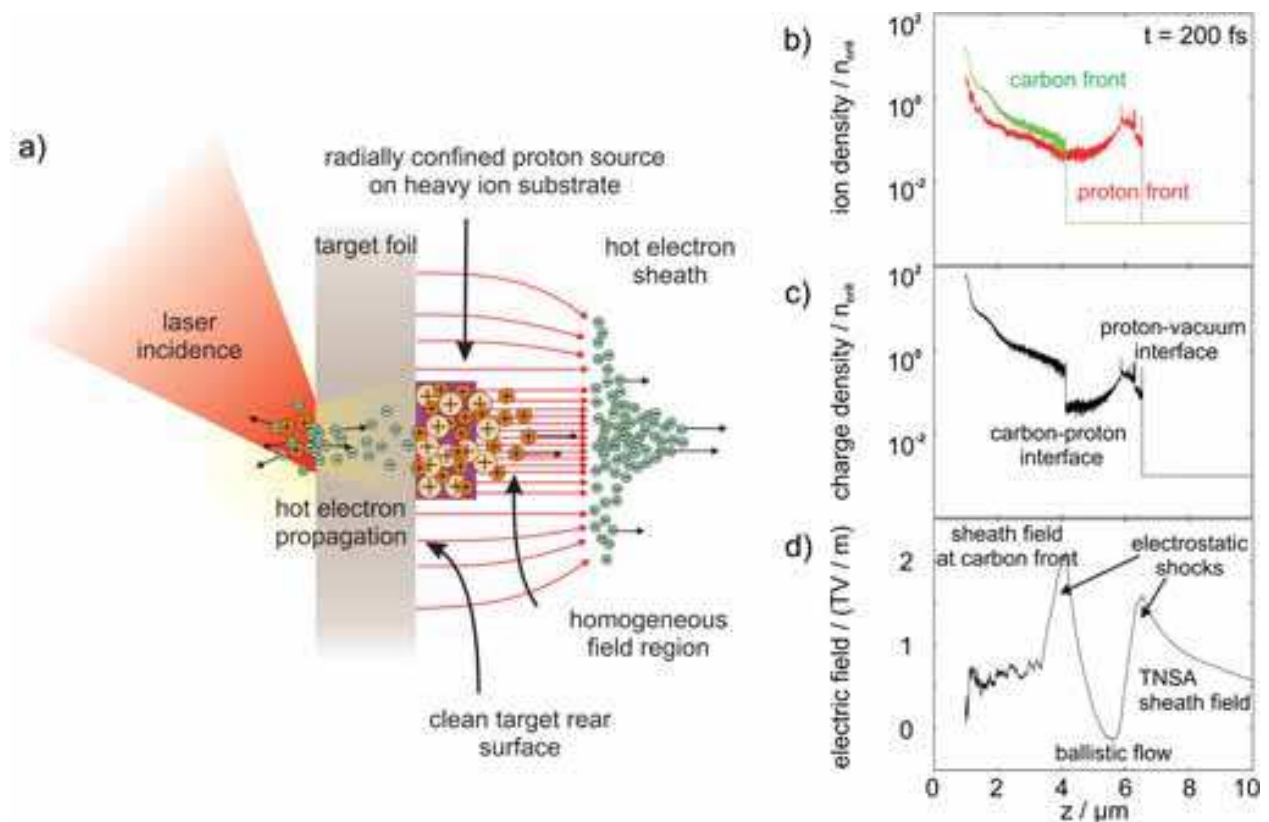
Fig. 14. The schematics of the Confined TNSA process (a) and results from a simulation of the acceleration process (b)–(d) at 200 fs. Simulation data courtesy of A.P.L. Robinson (Pfotenhauer, 2009; Robinson et al., 2009).

carbon boundary by the second sheath field, whereupon they immediately enter the zero-field region and remain in a state of motion of uniform ballistic flow. Note that the potential of charge separation for the spectral modulation of laser-accelerated ion beams had been identified in earlier works already (Tikhonchuk et al., 2005; Robinson et al., 2006).

The confined TNSA scheme has been confirmed for the first time experimentally by our group (Schwoerer et al., 2006; Pfotenhauer et al., 2008). Several other techniques for the generation of monoenergetic ion beams have been developed. These include the use of ultrathin Carbon layers for the generation of monoenergetic C^{5+} and C^{6+} beams (Hegelich et al., 2006), the generation of monoenergetic deuteron beams from droplet targets (Ter-Avetisyan et al., 2006), and active beam shaping and spectral selection of standard-TNSA generated proton beams using a fs-laser driven micro lens (Toncian et al., 2006).

4.3 Experimental studies of laser-ion acceleration
4.3.1 Setup for ion acceleration via confined TNSA
Fig. 15 (a) shows the schematics of the experimental realisation of the Confined TNSA regime. Like for standard TNSA ion acceleration, an intense laser pulse is focused onto a thin metal foil in order to generate the hot electron sheath at the target rear side. Contrary to the regular TNSA, however, a small microdot (typically made from polymer) has to be positioned exactly opposite to the laser incidence position. This is realized by manufacturing targets carrying an array of microdots on their backside and translating the target with the help of an adequate alignment procedure. Furthermore, since the ion source in standard

TNSA is constituted from contaminants being present also under vacuum, a target backside cleaning must be carried out straight before the main laser shot which has to remove the adsorbates completely but must preserve the dot. For that purpose, we use an additional, weakly focused, ns-pulsed, ablation laser.
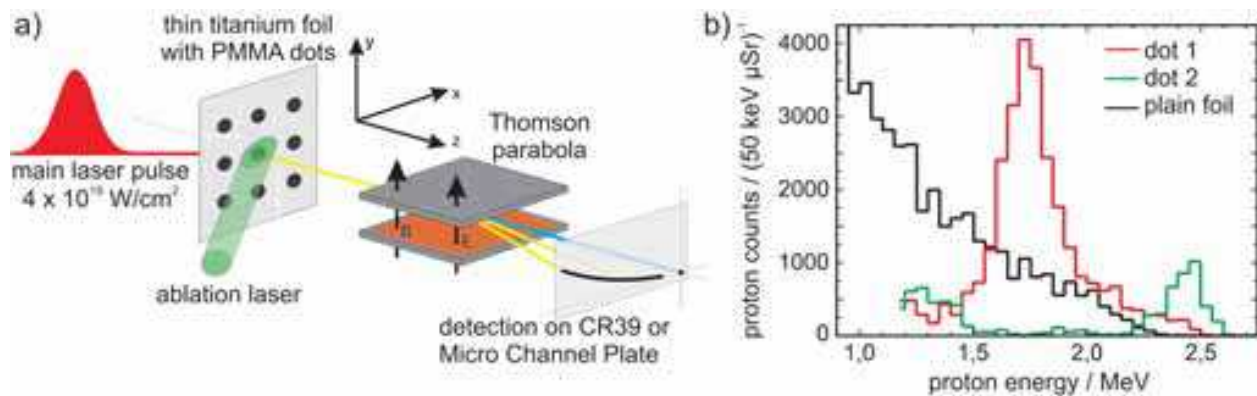

Fig. 15. Experimental setup (a) and generated proton spectra (b) of Confined TNSA. The main laser pulse hits the thin foil target at the front side exactly opposite to a micro-dot. Protons from the dot are accelerated within the central, homogeneous field region of the TNSA field and analysed with a Thomson spectrometer. The ions can be detected either with CR39 track detection plastics or an online imaging system (MCP). A second laser, which hits the target on the back side concentrically with respect to the main laser, is used for the cleaning of the target from residual contamination layer protons.

All that is highly non-trivial: The manufacturing of reproducible and resistant microstructures on a 2–5 micrometer thin metal foil represents a great engineering challenge. Secondly, the alignment of the dots with the laser incidence is equally difficult and crucial, as this means to align the laser pulse impinging on the target front side with something that is visible only from the back side. For this purpose, the back side was observed with a long distance microscope with micrometer resolution. In addition, the ablation laser must hit the target backside co-centred with the main laser incidence position. This laser was weakly focused on the surface with a diameter of typically $d_{\mathrm{foc}} \approx 600\ \mu$m in order to cover the whole proton source area around the dot. It was found that the careful regulation of the fluence of the ablation laser Φ_{abl}, the number of ablation shots and the time delay before the main laser pulse have a strong impact on the reliability of the generation narrowband proton beams (Pfotenhauer et al., 2008; Pfotenhauer, 2009).

The generated proton and ion beams propagated towards the spectrometer chamber, where the beam diameter was reduced by a pinhole of variable size (0.3 mm, 1 mm or 3 mm). Subsequently, the limited beam was dispersed in a Thomson spectrometer. The energy resolution of the spectrometer was defined by the pinhole diameter to $\Delta W_{\mathrm{res}} = 50$ keV for 1 MeV protons using the 1 mm aperture. The particles were detected either with CR39 track detection plates or with an online imaging system based on micro channel plates (MCP) in a chevron setup.

4.3.2 Microstructured targets

The fabrication of adequate targets for Confined TNSA was realized in two steps. First, a layer of PMMA was applied on a thin carrier foil. The polymer was evenly spread on the

back side of the foil using a spin coating technique, which yielded well-defined layer thicknesses of 50–1000 nm.

In a second step, the coated target surface was microstructured via laser ablation using a focussed Ti:Sapphire laser beam (λ_L = 800 nm, W_L = 5 μJ, τ_L = 60 fs) with 1 kHz repetition rate. Square dots with a minimum size of 10 × 10 μm^2 were carved out from the PMMA surface, see Fig. 16 (a) and (b). Alternatively, target microstructuring was also performed via photo-lithography. In this case, the PMMA surface was irradiated with a UV argon-fluoride excimer laser (λ_L = 193 nm, W_L = 3 mJ, τ_L = 15 ns) through a custom-designed chrome-layered quartz glass mask. An example target is shown in Fig. 16 (c).

The PMMA microstructures fulfil all the requirements put forth by the Confined TNSA model. That is, they provide a radially limited proton source in the form of a compound with a heavier ion species (carbon) to be subject to the charge separation effects discussed above. Together with a robust target cleaning procedure they provide the means to pursue monoenergetic proton acceleration.
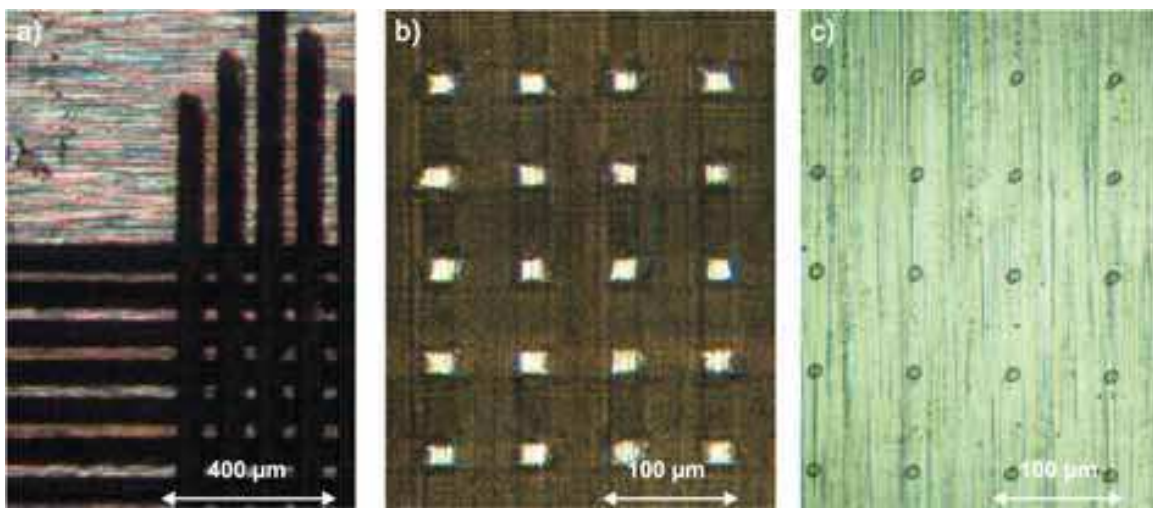

Fig. 16. (a) + (b) Fabrication of microstructured targets via fs-laser ablation. For the fabrication of microstructured targets suitable for Confined TNSA, a layer of polymer (PMMA) with 50 − 1000 nm thickness was first deposited to titanium foils via spin coating. From the polymer-covered surface, small square dots of 20×20 μm^2 extent and 80 μm separation were "carved out" with the help of a femtosecond laser system. Fig. (a) clearly shows the perpendicular carving traces ranging into the polymer. Note the well-defined carving edges typical for fs-ablation. (c) Lithography targets. Round dots of 10 μm diameter with 80 μm separation were generated via UV-lithography with a pulsed excimer laser. This alternative technique allows for a more flexible fabrication of micro-dots, which are, however, considerably more sensitive to target cleaning than those produced with the femtosecond system.

4.3.3 Properties of narrowband ion beams

Figure 14 (b) shows exemplary proton spectra obtained from microstructured targets. Spectra were obtained from the irradiation of PMMA micro-dots after 10 consecutive laser ablation shots at the threshold fluence of Φ_{abl} = 1.2 J/cm^2 (red and green lines). In comparison to plain (unstructured) 5 μm Titanium foil without laser ablation of

contaminants (black line), the proton spectra from the polymer dots show distinct peaks at W_{center} = 1.7 MeV with an energy width of ΔW_{FWHM} = 0.25 MeV = 15% for dot 1 and W_{center} = 2.5 MeV with ΔW_{FWHM} = 0.2 MeV = 8 % for dot 2. The ablation has suppressed the parasitic low-energy component of the spectrum and enables the acceleration of monoenergetic protons from the confined dot source. Narrowband features appear consistently once an ablation threshold fluence of Φ_{thr} = 1.2 J/cm² at 532 nm is surpassed (Pfotenhauer et al., 2008). In contrast, the laser-irradiation of a plain Titanium foil (black line) yields a thermal distribution typical for standard TNSA. The contrast between proton peak and thermal spectrum is typically 4:1. The peaks itself stand out well from the background signal, they contain typically between 80–90 % of all protons.

The number of protons contained in the spectra of Fig. 14 (b) was limited by the solid angle of observation of the setup, 1 μsr, which in turn was determined by a 1 mm pinhole in front of the ion spectrometer. In previous experiments (Schwoerer et al., 2006), the divergence of proton beams from plain, unstructured foils was measured to be much larger, amounting to 360 msr at a proton energy of 1.6 MeV, or 60 msr at 2.5 MeV, which implies that only a small fraction of the total number of protons is actually detected.

However, simulation studies confirm that the narrow band feature in the spectrum is not limited to the small angle of observation but appears equally over the whole emission angle (Robinson et al., 2009). Another set of 2D-PIC simulations carried out by Timur Esirkepov indicates that the angle of emission for micro-dots is approximately 24 msr for a peak at 1.1 MeV and hence somewhat lower than the experimental values measured for plain targets. Using this solid angle of 24 msr as a conservative estimation for the total number of protons, one finds that the peak of dot 1 of Fig. 14 (b) contains about $N_p \approx 4.1 \cdot 10^8$ in the FWHM peak. From integration over the narrowband spectrum it follows that the *conversion efficiency* of laser energy (0.78 J on target) into kinetic energy of protons amounts to $\eta_p = 1.4 \cdot 10^{-4}$ for the FWHM peak.

4.3.4 Peak position scaling

A subject of great interest for the generation of monoenergetic proton beams is the scalability of the acceleration mechanism to higher laser powers. Having established the high degree of reproducibility discussed in the previous section, the peak parameters for many hundred monoenergetic spectra were evaluated as a function of the main laser pulse energy, keeping all other parameters (dot dimensions, focal spot size, laser pulse duration, prepulse conditions, ablation conditions etc.) fixed. It shall be emphasized that the use of an online detection system like an MCP clearly facilitates the collection of such large amounts of data. Fig. 17 shows a subset of data where the main laser pulse energy was increased from 0.5 to 0.8 J on target (black squares). The four data points comprise a total of 140 spectra, all taken from 5 μm titanium foils carrying PMMA dots of 200 nm thickness after 10 consecutive shots of ablation at the threshold fluence Φ_{thr} = (1.2 ± 0.3) J/cm². Statistical analysis yields that the average peak position increases from 1.42 to 1.63 MeV over this energy range. The error bars represent the standard deviation of the sub-sets and thus give a measure for the shot-to-shot fluctuation. Note that the energy range covered by the four data points was constrained by the available laser energy (upper boundary) and the detection range of the spectrometer (lower boundary). The four data points strongly suggest a linear dependency between the peak position and the laser energy for the observed energy range.
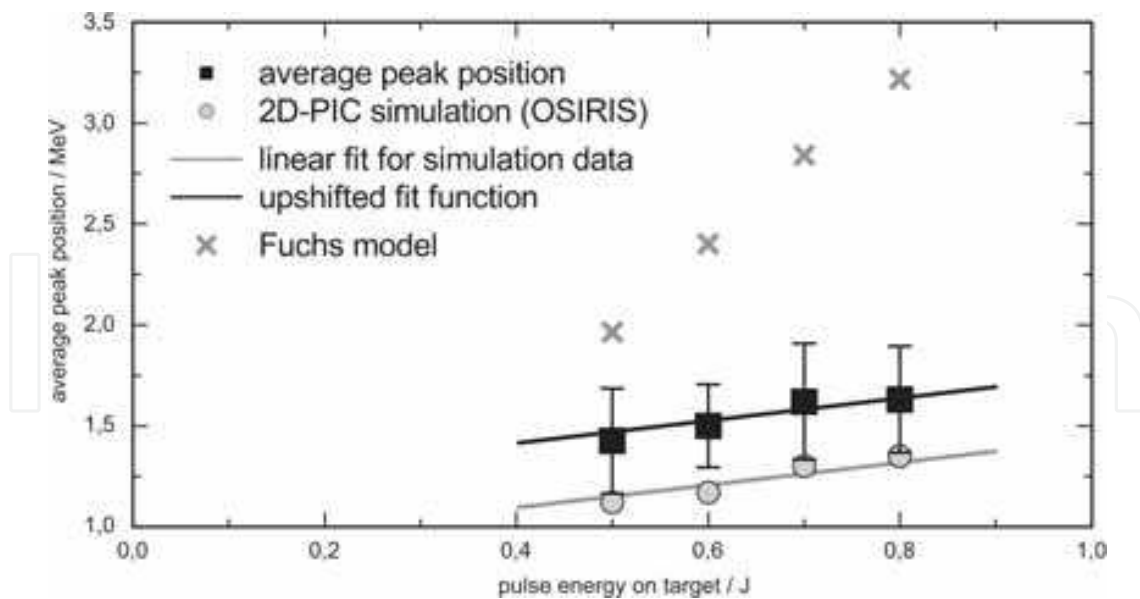
Fig. 17. Dependency of monoenergetic proton peak position on the laser pulse energy. The laser pulse energy on target was varied from 0.5 to 0.8 J, which corresponds to intensities of $2.9 - 4.7 \cdot 10^{19}$ W/cm². Consequently, the average peak position rose from 1.42 to 1.63 MeV (black squares). All other parameters were kept fixed. The four data points include a total of 140 monoenergetic spectra, lending sufficient statistical significance to the results. The error bars represent the standard deviation of the statistical sample and delineate the shot-to-shot fluctuation. The observed proportionality is excellently reproduced by 2D-PIC simulations carried out for our experimental parameters (grey circles). The calculated peak positions lie slightly outside the standard deviation, but are well within statistical range of the sample sets. All previous scaling laws refer to the cutoff energy of thermal spectra from plain foils and fail to account for our data. For example, the model by (Fuchs et al., 2006) predicts much higher energies and a steeper slope (grey crosses) for the current parameters.

In order to support this evidence, we carried out 2D PIC simulations for the different laser energies applied in the statistical analysis. The results are shown in Fig. 17 as grey circles: Similar to the experimental data, the calculated peak position increases in a linear manner, rising from 1.17 to 1.35 MeV over the observed energy interval. An additional simulation was carried out for a pulse energy of $W_L = 15$ J in order to investigate whether this behaviour holds true also at higher laser energies. This run yielded a monoenergetic peak at 9.3 MeV in very good agreement with the linear extrapolation of the four calculated spectra between 0.5 and 0.8 J. Together, the five simulation data points follow the linear function

$$W_{\text{peak}} / \text{MeV} = 0.56 \cdot W_L / \text{J} + 0.87, \tag{27}$$

represented by the grey line in Fig. 17. The numerical results appear systematically lower than the experimental values. However, it is striking how closely the slope of the simulation data matches that of the experimental data. The black line in Fig. 17 depicts the same linear fit function (27), upshifted only by 320 keV. This excellent accordance lends authority to the deduced linear scaling, which hence represents a scaling law for the generation of monoenergetic proton beams from microdot assisted laser proton acceleration.

The importance of this scaling law becomes evident when comparing it to other scalings proposed for laser proton acceleration. Various dependencies have been suggested to

connect the proton energy to the laser power or intensity (Mora, 2003; Fuchs et al., 2006; Schreiber et al., 2006; Robson et al., 2007), and it is known from previous measurements that for example the model by Fuchs et al. successfully predicts the observed maximum energies for standard TNSA conditions. However, all of these scaling laws refer solely to the cutoff energy of thermal spectra from plain foils. Contrarily, it has been shown above that the peak position from Confined TNSA does *not* coincide with the cutoff energy of the corresponding thermal spectra, but is bound to the slower heavy ion front. It is therefore not ad hoc intelligible if and how the peak formation scales with laser energy. Clearly, the thermal scaling laws cannot be expected to account for the peaks, and in fact a comparison of our data with the scaling law from (Fuchs et al., 2006) shows a strong discrepancy for the observed narrow parameter interval already. This deviation is illustrated by the grey crosses in Fig. 17, showing that the model by Fuchs et al. predicts much higher energy values and an approximately 8 times steeper slope. Eq. (27) hence represents the first scaling law specifically for monoenergetic proton spectra, and verifies for the first time that techniques for the generation of intrinsically monoenergetic ion beams can be extrapolated to higher laser energies. Furthermore, it indicates that the peak energy scales slower than the thermal cutoff energies and that thermal energy scalings overestimate the potential of laser ion acceleration when it comes to monoenergetic beams, which are the prerequisite for most applications. Nonetheless, today's capability of reliably generating $\sim 10^9$ quasi-monoenergetic protons with less than 10 % bandwidth by means of a scalable technique marks an important step towards applications.

5. Summary and outlook

The main motivation of investigating laser-based particle acceleration is the possibility of using much higher accelerating fields, resulting in smaller accelerators. Thus, before giving a small outlook onto possible applications, it seems well worthwhile to summarize the achievements of laser accelerators as of today and to compare them to benchmarks of conventional accelerators. Even though this is a tempting task, it should be noted that a mere comparison of numbers might be misleading, as certain quantities have been defined with certain applications in mind. In conventional accelerator science, comparisons are often made by historically grown "figures-of-merit" (FOMs): current, transverse emittance (focusability), longitudinal emittance (compressibility) and brilliance. Without doubt, these FOMs have their qualifications but should be seen in their specific context. For instance, the quantity "spectral peak brilliance", defined as particles per pulse length, per unit area, per unit solid angle and per relative spectral bandwidth, is often used to compare synchrotron facilities (cf. Sec. 5.2). It presupposes that the electron beam can be focused to a small and collimated beam, which in turn already requires a small spectral bandwidth in order to avoid chromatic aberration. In addition, peak brilliance is rather relevant for single shot applications where a sufficiently strong signal must be provided by a single shot. This measure fails, however, if a large number of shots is required, as is the case for example in most collider experiments, a situation which would be captured better by the "average brilliance".

In view of the relatively young field of laser-particle acceleration, it seems more sincere to provide rather "primary" quantities: peak energy, spectral width, bunch charge, pulse duration, bunch repetition rate, beam pointing, beam size and divergence. Nonetheless, it is

instructive to dare the comparison in the conventional accelerators' "own terms", so-to-say, in order to point out the advantages and disadvantages of the novel approach introduced in this chapter. After presenting in the following first a status of the current abilities of laser-produced particle beams, we will then point the spotlight onto a few prominent and important application-related research fields.

5.1 Comparison to conventional accelerators

Generally, laser-plasma accelerators produce significantly shorter pulses than conventional ones, which follows directly from the use of ultra-short laser pulses as drivers. This is a key feature for laser-produced particle beams and leads in general to the effect, that all "peak" beam quantities are comparably high. Thus, laser-based accelerators are predestined for time-resolved or single-shot applications. On the other hand, average beam properties are typically quite low for laser-based accelerators since today's laser repetition rates are limited to 10 Hz, whereas conventional accelerators can operate up to MHz rates. This is likely to continue in the future since current CPA laser technology cannot handle the required average optical powers and thermal loads.

A second major difference is the reduced acceleration length, which is generally seen as the most promising aspect of this new generation of particle accelerators. This may potentially reduce the dimensions of accelerator facilities significantly — which is an important economic argument. On the other hand, due to their meter-scales, conventional accelerators allow for relatively easy and independent beam control. In particular, they consist not only of accelerating units (RF resonators) but also of beam forming devices (e.g. quadrupole magnets). Currently, it is quite difficult to transfer similar schemes to laser-plasma accelerators. In the bubble regime of electron acceleration, there are transverse electric fields present which accomplish longitudinal bunching and transverse beam focusing. However, this is inherently coupled to the acceleration process — being far away from external control. The Confined TNSA with the use of two ion species and a region of zero-field strength is similar but resembles as intentional, artificial manipulation of the plasma. On top of that, very recently, we were able to realize a staged acceleration setup, where at a second target foil a second TNSA field was generated which enabled us to post-accelerate protons from a first foil target (Jäckel, 2009). Depending on the distance of the two target foils and timing of the TNSA fields, one can select the energy of the protons being post-accelerated. This temporal gating allows for spectral control, and the staging itself is an efficient method to increase the proton energy. Thus, glancing over the rapid progress in the recent years in the domain of laser-based particle acceleration, the challenges of beam control will be taken and turn into productive future developments.

In addition to such general rating, we will now present relevant beam parameters. Regarding laser-driven electron acceleration, 1 GeV electron beams can be generated within 3 cm (Leemans et al., 2006) whereas typical synchrotrons, operating at a few GeV, have diameters of up to 100 m. This milestone clearly shows the general potential of laserbased particle acceleration as more compact accelerators. The pulse lengths are also very promising. Although exact pulse length measurements are still pending, upper limits are determined to 50 fs (van Tilborg et al., 2006), and simulations promise bunch durations below 10 fs (Pukhov & Meyer-ter-Vehn, 2002). Conventional accelerators usually produce ns long pulses, sub-ps pulses are extremely difficult to generate. Bunch charges from laserplasma accelerators are typically on the order of several 10 pC. In contrast, conventional

accelerators can produce several 10 nC. This large discrepancy of 3 orders of magnitude is a serious problem for many applications with laser-based accelerators, and possible solutions are currently investigated. However, the peak current as a combination of both measures is at least comparable to conventional accelerators. Considering the energy spread, typical results for laser-plasma accelerators are 5 % of the peak energy. However, this value is mostly instrument-limited, thus the actual energy spread could be smaller. A relative spread of the order of 10^{-3} would suffice for most applications. Thus, the energy spread is also a point on top of the agenda. Another rather open question is the transverse emittance, which determines the focusability of the beams. From our measurements, the smallest beam divergence is $\sigma' = 2$ mrad. Assuming a source size of $\sigma \sim 2 \; \mu$m (Pukhov & Meyer-ter-Vehn, 2002), yields a transverse emittance of $\varepsilon_\perp = \sigma^2 \sigma'^2 \gtrsim 10^{-5}$ mm^{2}mrad^2. This corresponds to a normalized, cold-beam transverse emittance of $\varepsilon_n = \gamma\beta\sqrt{\varepsilon_\perp} \sim 0.1$–$0.5 \; \mu$m for the obtained electron energies of up to ~ 70 MeV. Very recent direct measurements show the transverse emittance to be of the order of $\varepsilon_n \sim 5 \; \mu$m, which must be considered rather as an upper limit. If the normalized emittance would be below 1 μm, it would be comparable to conventional accelerators. We observed a pointing stability of the beams of 40 mrad which is much too large for applications. Other groups have shown electron beams with stable beam pointing of about 1 mrad which is, especially in combination with beam focusing elements, sufficient for further use of the beams (cf. Sec. 5.2).

Regarding ion acceleration, we will exclusively consider proton beams generated via Confined TNSA as the currently only method to reproducibly generate intrinsically narrowband ion spectra. The determined charge of $4 \cdot 10^8$ protons is of the same order as the one of electron beams, thus a similar discrepancy arises. The currently generated proton beams show peaks at about 2 MeV energy with about 10 % bandwidth. This must be seen as proof-of-principle experiment and is too early to compete with conventional ion accelerators. With today's available laser technology, the 10vMeV range can be achieved easily. Furthermore, simulations suggest that the absolute peak width saturates with increasing peak energy, which might reduce the relative width effectivly. The pulse duration may be estimated from the length of the zero-field region in Fig. 14 (d). For 2 MeV proton energy, a length of 1 micron corrensponds to a time of 300 fs. However, this pulse will disperse in free space propagation simply due to its different velocities. This problem disappears if the beams move relativistically with velocities close to *c*. The opening angle was also derived from simulations to 24 msr which corresponds to a divergence half angle of 87 mrad. An estimation of the transverse emittance can be provided by taking into account the angle of emission and a proton source size determined by the diameter of the microdots (20 μm), which yields a transverse emittance of $\varepsilon_\perp \gtrsim 2$ mm^{2}mrad^2. The normalized emittance amounts then to $\varepsilon_n \gtrsim 0.1 \; \mu$m. For laser-plasma accelerators, transverse emittance values of $\varepsilon_n < 4 \cdot 10^{-3} \; \mu$m have been measured using mesh magnification techniques (Cowan et al., 2004). The herepresented estimate is larger but still outmatches the emittances of conventional accelerators by more than one order of magnitude (e.g. $\varepsilon_n \approx 3 \; \mu$m for the CERN SPS (Arduini et al., 2003)), which clearly indicates the potential benefits of laser driven particle acceleration already at this early stage.

The longitudinal emittance is defined as the product of the pulse duration and the energy spread, $\varepsilon_{long} = \Delta\tau_{pulse} \cdot \Delta W_{kin}$, and gives a measure for the re-compressibility of the particle beam, in analogy to the time-bandwidth-product of short laser pulses (cf. Sec. 2.1). For the

experiments under discussion, the FWHM energy spread of 0.2MeV together with an initial pulse duration of 300 fs yields a longitudinal emittance of $\varepsilon_{\text{long}} \approx 6 \cdot 10^{-8}$ eVs, which is an extremely low value. Even if the pulse duration is conservatively approximated by the lifetime of the TNSA sheath field of roughly 10 ps, one still finds a theoretical emittance of $\varepsilon_{\text{long}} \approx 2 \cdot 10^{-6}$ eVs, which is many orders of magnitude below the values achieved by conventional accelerators (e.g. $\varepsilon_{\text{long}} \approx 0.35$ eV s for CERN SPS (Arduini et al., 2003)).

Finally, the beam peak brilliance, defined as particle flux dN/dt per area dA, spectral bandwidth dW and solid angle $d\Omega$, may be estimated. Gathering all numbers, we ultimately end up with $B \sim 10^{27}$ eV^{-1}s^{-1}m^{-2}sr^{-1}. In comparison, the peak brilliance of CERN SPS amounts to $B_{\text{SPS}} = 5.3 \cdot 10^{24}$ eV^{-1}s^{-1}m^{-2}sr^{-1} according to the presented parameters.

Note, however, that a large acceleration facility like CERN SPS provides considerably more protons per pulse ($\approx 10^{11}$) at a 5 orders of magnitude higher peak energy (≈ 450 GeV) with a significantly smaller spectral bandwidth! The beam properties of the laser-produced proton beams discussed in this section should hence be recognized more as an illustration of the *complementary and unique physical regime* accessed by laser accelerators, rather than a competitive comparison between different machines aiming at the same parameters.

5.2 Short-pulsed radiation sources

Due to their short wavelengths, X-rays are suited to study the structure of matter on the atomic length scale. However, for many fundamental processes like phase-transitions, it is necessary to have a time-resolving investigation method. Pump-probe experiments can do so, but require i) two short pulses with ii) a precise delay between them. Conventional means to produce X-rays are x-ray tubes and synchrotron sources. The latter have matured in the recent decades and are to date the most intense sources which attract large used communities. However, up to now they rely on conventional accelerators and are large, expensive facilities. Furthermore, to achieve sufficient time resolution, huge efforts must be undertaken. Nowadays, only two facilities can produce ultra-short X-ray pulses.

For this particular application, the use of laser-accelerated electron bunches for the production of synchrotron radiation seems very promising. Firstly, the large and expensive conventional accelerator could be replaced. Secondly and most important, the produced electron pulses are inherently ultra-short and ultimately synchronized to an ultra-short pulsed laser system. By that, the demands for pump-probe experiments are perfectly met. Furthermore, the recent realization of short-pulse capabilities with conventional accelerator techniques, facing immense problems to be overcome and going to technological limits, shows the demand of scientists for short-pulse synchrotron radiation facilities.

We have shown in a proof-of-principle experiment the production of synchrotron radiation by sending laser-accelerated electrons through a magnetic undulator for the first time (Schlenvoigt et al., 2008). This technique is now used for precise characterization of electron beams (energy, energy spread and emittance) as well as — depending on the electron beams — for the production of short VUV pulses. In the near future, the wavelength range will be extended to soft X-rays. Furthermore, an experiment to measure the pulse duration should be carried out as well as a proof-of-principle experiment for the pump-probe capabilities of this scheme. In addition, the FEL operation will be tested which requires low transverse emittance, low energy spread and high peak current. The undulator may be either operated in the SASE-FEL mode, or eventually as FEL seeded by a coherent laser-driven source.

A different laser-driven source of X-rays is Betatron radiation (Rousse et al., 2004). In this regime, electrons undergo transverse plasma oscillations in the plasma channel. Again, short radiation pulses are produced, but in a compact single-stage setup. This may have advantages, but a control of the radiation is difficult. To date, rather broadband radiation is produced, being used to diagnose the average electron motion in the plasma during the acceleration process (Phuoc et al., 2006; Kneip et al., 2008). For future applications, separated accelerator-radiator schemes are conceivable. However, in contrast to laser-driven FELs, no coherence will be possible.

5.3 Cancer therapy

Radiation therapy is a widely-used method in cancer treatment. It is commonly used for the treatment of tumours in the vicinity of risk organs, where surgery would be too difficult, and can be used as palliative means. Especially the use of high-energy ion beams has several advantageous aspects compared to Bremsstrahlung or electron beams. The absorption behaviour is such that the ions propagate with quasi-constant differential energy loss up to a point where the particle is already sufficiently slow and different interaction mechanisms lead to sudden stopping. This leads to well-defined penetration depths and the so-called Bragg peak at the end of the path: a maximum of energy deposition per unit propagation length. In addition, the beams experience only little side scattering and have thus a relative sharp contour. An implication for oncology is that the healthy tissue surrounding the tumour is exposed to much less dose if an ion beam is used. Furthermore it was found that the relative effectiveness of cell damage induced by ion beams, compared to Bremsstrahlung, is up to a factor of 6 higher in the Bragg peak.

Currently, there are only about 30 ion beam therapy (IBT) facilities worldwide in operation. This is on the one hand caused by the size of the accelerators in order to produce the required particle beams, e.g. ~ 200 MeV protons or ~ 1 GeV carbon ions. On the other hand, the additional necessary infrastructure to guide the beam from the accelerator to the patient is substantial and relies on large, heavy magnetic deflection devices, precisely movable around the patient. Both requires large buildings, shielding and high investments.

The promise of laser accelerators, then, is that the whole accelerator setup is significantly smaller than that of conventional devices, and thus the accelerator could in principle be located very close to the patient or even aligned and rotated around it. The main advantage would be that the only thing to be guided over longer distance is laser light, which means considerably less radiation hazard and hence reduces the shielding requirements. Besides that, the short and intense radiation pulses might have a different — and possibly better — radio-biological effectiveness. It is currently debated if the much higher peak dose rate induces DNA damage in a different way. Above that, one can image a kind of pump-probe scheme: A first pulse generates DNA damage in the cells. The damages are recognized by the cell and repair mechanisms are started. Now it could be possible to apply the second pulse at a time when the cell is vulnerable. But these are just ideas which have to be investigated.

Based in the reliable generation of electron beams from gas jet targets (see Sec. 3.3), we performed initial experimental investigation of biological radiation effects of laser-generated particle beams (Beyreuther et al., 2009). A first goal was to establish an experimental setup which allowed us to perform in-vitro irradiation of standard cell samples where the applied dose can be monitored simultaneously. This is a crucial feature for several reasons: The laser-plasma accelerator's performance can be measured, e.g. the amount of shot-to-shot

fluctuations or transient drifts of the dose (cf. Sec. 3.3). Secondly, since online monitoring systems are implemented in all medical devices, it is reasonable to begin with the development at an early stage of innovation process. We used several dose detectors at the same time which rely on different effects, which allowed us to establish reliable dose measurements of ultra-short radiation pulses.

In a second step we conducted irradiation experiments of human cell samples. Two different standard cell lines, one for normal tissue and one for tumour tissue were irradiated. The dose was varied in order to investigate the cell response as function of dose. Two different kinds of biological response were investigated: The formation of DNA double strand breaks, induced by the irradiation (which is a primary response) and the total cell survival (which is a final goal but may be different to primary DNA damage due to DNA repair mechanisms). For methodical reasons, cell samples were also irradiated with cw Bremsstrahlung from a reference source. Future work will extend these investigation to more cell lines and to the irradiation with laser-accelerated ion beams. For a more detailed review, please see (Beyreuther et al., 2009).

5.4 Fast ignition

For future energy production, only nuclear fusion has sufficient long-term capabilities. This may be either the sun itself or man-made nuclear fusion. For the latter, two main technologies are know: magnetic confinement and inertial confinement. For inertial confinement fusion, e.g. see the textbook (Atzeni & Meyer-ter-Vehn, 2004), up to hundreds of energetic (multi-kJ) long-pulse (ns) lasers are focused onto a hollow fuel capsule of a few mm diameter. A plasma corona is created where particles are heated. The hot expanding plasma pushes (due to momentum conservation) the fuel capsule into itself, it implodes. When the shell reaches its centre, it gets compressed and heated. In the "pure" ICF regime, pressure, temperature and duration of being compressed suffice for ignition of the fusion process.

This is similar to a Diesel engine. The demand is to achieve high compression in a very symmetric manner. However, the coronal plasma shows instabilities which complicate the compression. A further option is to ignite the compressed and heated core by external means, like the fuel vapour in a petrol engine with spark-ignition. This is called fast ignition (FI).

For fast ignition, several possibilities are debated and will be investigated in the next years: Heating by laser-produced electron beams, heating by laser-produced light ions, heating by laser-driven shock waves or heating by heavy-ion beams (from conventional accelerators). Ignition by laser-accelerated electron beams demands very contrary beam characteristics as radiation generation (cf. Sec. 5.2). The goal is to generate a huge number of electrons with energies below a few MeV in a small beam. Electrons with higher energies would not deposit all their energy in the small compressed core, hence initial laser energy would be wasted. But since the total energy to be deposited is fixed, the number of electrons is the only free parameter. For this reason, LWFA-based schemes do not seem to be applicable.

One route is to accelerate electrons directly from the coronal plasma. Problems arise from the quite long distance from the acceleration zone to the core. Electron beams would have to be well-collimated in order not to miss the core, and much electron beam energy will be absorbed in the coronal plasma. Hence it is desired to bring the driving laser closer to the core. A principle option is using a very intense laser pulse of PW power which can push the coronal plasma aside (hole-boring). Another possibility is to attach a solid cone to the fuel capsule. This cone endures the compression phase due to its mass inertia. Inside the cone,

there is no coronal plasma. Then, a short laser pulse is focused into the cone where an electron beam is generated. However, like for ion acceleration, a preplasma filling of the cone inhibits efficient electron acceleration (Baton et al., 2008). This demand for high-contrast laser pulses will be even more difficult to satisfy than for TNSA, since the required pulse energies are higher and the pulses longer. For ion-driven FI, there are even more open questions. Based on the results with a PW laser (Snavely et al., 2000) where ~ 10 % of laser energy were transferred into a proton beam (50 J in the particle beam, from 500 J in the laser pulse), several concepts have been developed. However, and this is a general problem also for electron-driven FI, sufficiently powerful laser systems are not yet ready or have performance problems like a poor temporal contrast which generates a preplasma and attenuates the interaction.

6. Acknowledgements

7. References

Alfvén, H. (1939). On the Motion of Cosmic Rays in Interstellar Space. *Physical Review*, Vol. 55, pp. 425–429

Arduini, G.; Baudrenghien, P.; Bohl, T.; Collier, P.; Cornelis, K.; Höfle, W.; Linnecar, T.; Shaposhnikova, E.; Tückmantel, J. & Wenninger, J. (2003). The LHC Proton Beam in the CERN SPS: an Update. *Proceedings of the 2003 Particle Accelerator Conference.*, pp. 1718–1720, accelconf.web.cern.ch/accelconf/p03/PAPERS/TPPB050.pdf

Atzeni, S. & Meyer-ter-Vehn, J. (2004). *The physics of inertial fusion*, Oxford University Press, ISBN 0198562640, Oxford

Baton, S.; Koenig, M.; Fuchs, J.; Benuzzi-Mounaix, A.; Guillou, P.; Loupias, B.; Vinci, T.; Gremillet, L.; Rousseaux, C.; Drouin, M.; Lefebvre, E.; Dorchies, F.; Fourment, C.; Santos, J. J.; Batani, D.; Morace, A.; Redaelli, R.; Nakatsutsumi, M.; Kodama, R.; Nishida, A.; Ozaki, N.; Norimatsu, T.; Aglitskiy, Y.; Atzeni, S. & Schiavi, A. (2008). Inhibition of fast electron energy deposition due to preplasma filling of cone-attached targets. *Physics of Plasmas*, Vol. 15, p. 042706

Beyreuther, E.; Enghardt, W.; Kaluza, M.; Karsch, L.; Laschinsky, L.; Lessmann, E.; Nicolai, M.; Pawelke, J.; Richter, C.; Sauerbrey, R.; Schlenvoigt, H.-P. & Baumann, M. (2009).

Establishment of technical prerequisites for cell irradiation experiments with laser accelerated electrons. *Medical Physics*, accepted for publication

Brunel, F. (1987). Not-so-resonant, Resonant Absorption. *Physical Review Letters*, Vol. 59, p. 52

Cowan, T.; Fuchs, J.; Ruhl, H.; Kemp, A.; Audebert, P.; Roth, M.; Stephens, R.; Barton, I.; Blazevic, A.; Brambrink, E.; Cobble, J.; Fernández, J.; Gauthier, J.-C.; Geissel, M.; Hegelich, M.; Kaae, J.; Karsch, S.; Le Sage, G. P.; Letzring, S.; Manclossi, M.; Meyroneinc, S.; Newkirk, A.; Pépin, H. & Renard-LeGalloudec, N. (2004). Ultralow Emittance, Multi-MeV Proton Beams from a Laser Virtual-Cathode Plasma Accelerator. *Physical Review Letters*, Vol. 92, p. 204801

Esarey, E.; Sprangle, P.; Krall, J. & Ting, A. (1996). Overview of plasma-based accelerator concepts. *IEEE Transactions on Plasma Science*, Vol. 24, No. 2, pp. 252–288

Esirkepov, T.; Bulanov, S.; Nishihara, K.; Tajima, T.; Pegoraro, F.; Khoroshkov, V.; Mima, K.; Daido, H.; Kato, Y.; Kitagawa, Y.; Nagai, K. & Sakabe, S. (2002). Proposed doublelayer target for the generation of high-quality laser-accelerated ion beams. *Physical Review Letters*, Vol. 89, p. 175003

Faure, J.; Rechatin, C.; Norlin, A.; Lifschitz, A.; Glinec, Y. & Malka, V. (2006). Controlled injection and acceleration of electrons in plasma wakefields by colliding laser pulses. *Nature*, Vol. 444, pp. 737–739

Fuchs, J.; Sentoku, Y.; Karsch, S.; Cobble, J.; Audebert, P.; Kemp, A.; Nikroo, A.; Antici, P.; Brambrink, E.; Blazevic, A.; Campbell, E.M.; Fernandez, J.C.; Gauthier, J.-C.; Geissel, M.; Hegelich, M.; Pepin, H.; Popescu, H.; Renard-LeGalloudec, N.; Roth, M.; Schreiber J.; Stephens, R. & Cowan, T (2005). Comparison of laser ion acceleration from the front and rear surfaces of thin foils. *Physical Review Letters*, Vol. 94, p.045004

Fuchs, J; Antici, P; d'Humieres, E; Lefebvre, E; Borghesi, M; Brambrink, E; Cecchetti, C.A.; Kaluza, M; Malka, V; Manclossi, M; Meyroneinc, S; Mora, P; Schreiber, J; Toncian, T; Pepin, H & Audebert, P. (2006). Laser-driven proton scaling laws and new paths towards energy increase. *Nature Physics*, Vol. 2, No. 1, pp. 48–54

Fuchs, J.; Cecchetti, C.A.; Borghesi, M.; Grismayer, T.; d'Humieres, E.; Antici, P.; Atzeni, S.; Mora, P.; Pipahl, A.; Romagnani, L.; Schiavi, A.; Sentoku, Y.; Toncian, T.; Audebert, P. & Willi, O. (2007). Laser-foil acceleration of high-energy protons in small-scale plasma gradients. *Physical Review Letters*, Vol. 99, No. 23, p. 015002

Gahn, C.; Tsakiris, G.; Pukhov, A.; Meyer-ter-Vehn, J.; Pretzler, G.; Thirolf, P.; Habs, D. & Witte, K. (1999). Multi-MeV electron beam generation by direct laser acceleration in high-density plasma channels. *Physical Review Letters*, Vol. 83, No. 23, pp. 4772–4775

Geddes, C.; Toth, Cs.; van Tilborg, J.; Esarey, E.; Schroeder, C.; Bruhwiler, D.; Nieter, C.; Cary, J. & Leemans, W. (2005). Production of high-quality electron bunches by dephasing and beam loading in channeled and unchanneled laser plasma accelerators. *Physics of Plasmas*, Vol. 12, p. 056709

Geddes, C.; Nakamura, K.; Plateau, G.; Toth, Cs.; Cormier-Michel, E.; Esarey, E.; Schroeder, C.; Cary, J. & Leemans,W. (2008). Plasma-Density-Gradient Injection of Low Absolute-Momentum-Spread Electron Bunches. *Physical Review Letters*, Vol. 100, p. 215004

Gibbon, P. (2005). *Short pulse laser interactions with matter*, Imperial College Press, ISBN 1860941354, London

Gordienko, S. & Pukhov, A. (2005). Scalings for ultrarelativistic laser plasmas and quasi-monoenergetic electrons. *Physics of Plasmas*, Vol. 12, p. 043109

Hegelich, M.; Karsch, S.; Pretzler, G.; Habs, D.; Witte, K.; Guenther, W.; Allen, M.; Blazevic, A.; Fuchs, J.; Gauthier, J.-C.; Geissel, M.; Audebert, P.; Cowan, T. & Roth, M. (2002).

MeV ion jets from short-pulse-laser interaction with thin foils. *Physical Review Letters*, Vol. 89, p. 085002

Hegelich, M.; Albright, B. J.; Cobble, J.; Flippo, K.; Letzring, S.; Paffett, M.; Ruhl, H.; Schreiber, J.; Schulze, R. K. & Fernandez, J. C. (2006). Laser acceleration of quasi-monoenergetic MeV ion beams. *Nature*, Vol. 439, pp. 441–444

Henig, A.; Kiefer, D.; Markey, K.; Gautier, D.C.; Flippo, K.A.; Letzring, S.; Johnson, R.P.; Shimada, T.; Yin, L.; Albright, B.J.; Bowers, K.J.; Fernandez, J.C.; Rykovanov, S.G.; Wu, H.C.; Zepf, M.; Jung, D.; Liechtenstein, V.K.; Schreiber, J.; Habs, D. & Hegelich, M. (2009). Enhanced Laser-Driven Ion Acceleration in the Relativistic Transparency Regime. *Physical Review Letters*, Vol. 103, p. 045002

Hidding, B.; Amthor, K.-U.; Liesfeld, B.; Schwoerer, H.; Karsch, S.; Geissler, M.; Veisz, L.; Schmid, K.; Gallacher, J. ; Jamison, S. ; Jaroszynski, D.; Pretzler, G. & Sauerbrey, R. (2006). Generation of quasimonoenergetic electron bunches with 80-fs laser pulses. *Physical Review Letters*, Vol. 96, p. 105004

Honrubia, J.J.; Kaluza, M.; Schreiber, J.; Tsakiris, G. D. & Meyer-ter-Vehn, J. (2005). Laserdriven fast-electron transport in preheated foil targets. *Physics of Plasmas*, Vol. 12, p. 052708

Jäckel, Oliver (2009). *Characterization of ion acceleration with relativistic laser-plasma,* PhD thesis, IOQ Jena, www.physik.uni-jena.de/ioq

Kaluza, M.; Schreiber, J.; Santala, M.I.K.; Tsakiris, G.; Eidmann, K.; Meyer-ter-Vehn, J. & Witte, K.-J. (2004). Influence of the laser prepulse on proton acceleration in thin-foil experiments. *Physical Review Letters*, Vol. 93, p. 045003

Karsch, S.; Osterhoff, J.; Popp, A.; Rowlands-Rees, T.; Major, Z.; Fuchs, M.; Marx, B.; Horlein, R.; Schmid, K.; Veisz, L.; Becker, S.; Schramm, U.; Hidding, B.; Pretzler, G.; Habs, D.; Grüner, F.; Krausz, F. % Hooker, S. (2007). GeV-scale electron acceleration in a gas-filled capillary discharge waveguide. *New Journal of Physics*, Vol. 9, p. 415

Kneip, S.; Nagel, S.; Bellei, C.; Bourgeois, N.; Dangor, A. E.; Gopal, A.; Heathcote, R.; Mangles, S.; Marques, J.-R.; Maksimchuk, A.; Nilson, P.M.; Phuoc, K.T.; Reed, S.; Tzoufras, M.; Tsung, F.; Willingale, L.; Mori, W.; Rousse, A.; Krushelnick, K. & Najmudin, Z. (2008). Observation of synchrotron radiation from electrons accelerated in a petawatt-laser generated plasma cavity. *Physical Review Letters*, Vol. 100, p. 105006

Kruer, W.L. & Estabrook, K. (1985). Jxb Heating By Very Intense Laser-Light. *Physics of Fluids*, Vol. 28, pp. 430–432

Kruer, W.L. (1988). *The physics of laser plasma interactions*, Westview Press, ISBN 0813340837, Boulder, CO, USA

Lau, Y.; He, F.; Umstadter, D. & Kowalczyk, R. (2003). Nonlinear Thomson scattering: A tutorial. *Physics of Plasmas*, Vol. 10, No. 5, pp. 2155–2162

Leemans, W.; Nagler, B.; Gonsalves, A.; Toth, Cs; Nakamura, K.; Geddes, C.; Esarey, E.; Schroeder, C. & Hooker, S. (2006). GeV electron beams from a centimetre-scale accelerator. *Nature Physics*, Vol. 2, No. 10, pp. 696–699

Malka, V.; Faure, J.; Glinec, Y.; Pukhov, A. & Rousseau, J. P. (2005). Monoenergetic electron beam optimization in the bubble regime. *Physics of Plasmas*, Vol. 12, p. 056702

Mangles, S.; Murphy, C.; Najmudin, Z.; Thomas, A.; Collier, J.; Dangor, A. E.; Divall, E. J.; Foster, P.; Gallacher, J.; Hooker, C. J.; Jaroszynski, D.; Langley, A. J.; Mori, W.; Norreys, P.; Tsung, F.; Viskup, R.; Walton, B. & Krushelnick, K. (2004). Monoenergetic beams of relativistic electrons from intense laser-plasma interactions. *Nature*, Vol. 431, pp. 535–538 (see also adjacent articles pp. 538–541 and pp. 541–544)

Meyer-ter-Vehn, J.; Pukhov, A. & Sheng, Zh.-M. (2001). Relativistic Laser Plasma Interaction, In: *Atoms, Solids, and Plasmas in Super-Intense Laser Fields*, Batani, D.; Joachain, Ch. J.; Martellucci, S. & Chester, A. N. (Ed.), pp. 167–192, Kluwer Academics / Plenum Publishers, ISBN 0306466155, New York

Modena, A.; Najmudin, Z.; Dangor, A.E.; Clayton, C.; Marsh, K.A.; Joshi, C.; Malka, V.; Darrow, C. B.; Danson, C.; Neely, D. & Walsh, F.N. (1995). Electron Acceleration From The Breaking Of Relativistic Plasma-Waves. *Nature*, Vol. 377, pp. 606–608

Mora, P. (2003). Plasma expansion into a vacuum. *Physical Review Letters*, Vol. 90, p. 185002

Mori, W. (1997). The Physics of the Nonlinear Optics of Plasmas at Relativistic Intensities for Short-Pulse Lasers. *IEEE Journal of Quantum Electronics*, Vol. 33, No. 11, pp. 1942–1953

Osterhoff, J.; Popp, A.; Major, Z.; Marx, B.; Rowlands-Rees, T.; Fuchs, M.; Geissler, M.; Hoerlein, R.; Hidding, B.; Becker, S.; Peralta, E. A.; Schramm, U.; Gruener, F.; Habs, D.; Krausz, F.; Hooker, S. & Karsch, S. (2008). Generation of stable, lowdivergence electron beams by laser-wakefield acceleration in a steady-state-flow gas cell. *Physical Review Letters*, Vol. 101, p. 085002

Pfotenhauer, S.; Jäckel, O.; Sachtleben, A.; Polz, J.; Ziegler, W.; Schlenvoigt, H.-P.; Amthor, K.- U.; Kaluza, M.; Ledingham, K.; Sauerbrey, R.; Gibbon, P.; Robinson, A. & Schwoerer, H. (2008). Spectral shaping of laser generated proton beams *New Journal of Physics*, Vol. 10, p. 033034

Pfotenhauer, Sebastian (2009). *Generation of monoenergetic ion beams with a laser accelerator*, PhD thesis, IOQ Jena, www.physik.uni-jena.de/ioq

Phuoc, K.T.; Corde, S.; Shah, R.; Albert, F.; Fitour, R.; Rousseau, J.P.; Burgy, F.; Mercier, B. & Rousse, A. (2006). Imaging electron trajectories in a laser-wakefield cavity using betatron x-ray radiation. *Physical Review Letters*, Vol. 97, p. 225002

Pukhov, A. & Meyer-ter-Vehn, J. (2002). Laser wake field acceleration: the highly non-linear broken-wave regime. *Applied Physics B*, Vol. 74, No. 4-5, pp. 355–361

Robinson, A.; Bell, A. R. & Kingham, R. (2006). Effect of target composition on proton energy spectra in ultraintense laser-solid interactions. *Physical Review Letters*, Vol. 96, p. 035005

Robinson, A. & Gibbon, P. (2007). Production of proton beams with narrow-band energy spectra from laser-irradiated ultrathin foils. *Physical Review E*, Vol. 75, p. 015401

Robinson, A.; Gibbon, P.; Pfotenhauer, S.; Jäckel, O. & Polz, J. (2009). Scaling of the proton density reduction scheme for the laser acceleration of proton beams with a narrow energy spread. *Plasma Physics and Controlled Fusion*, Vol. 51, p. 024001

Robson, L.; Simpson, P. T.; Clarke, R. J.; Ledingham, K.; Lindau, F.; Lundh, O.; McCanny, T.; Mora, P.; Neely, D.; Wahlström, C.-G.; Zepf, M. & McKenna, P. (2007). Scaling of proton acceleration driven by petawatt-laser-plasma interactions. *Nature Physics*, Vol. 3, pp. 58–62

Rousse, A.; Phuoc, K.T.; Shah, R.; Pukhov, A.; Lefebvre, E.; Malka, V.; Kiselev, S.; Burgy, F.; Rousseau, J.P.; Umstadter, D. & Hulin, D. (2004). Production of a keV x-ray beam from synchrotron radiation in relativistic laser-plasma interaction. *Physical Review Letters*, Vol. 93, p. 135005

Rowlands-Rees, T.; Kamperidis, C.; Kneip, S.; Gonsalves, A.; Mangles, S.; Gallacher, J.; Brunetti, E.; Ibbotson, T.; Murphy, C.; Foster, P.; Streeter, M.J.V.; Budde, F.; Norreys, P.; Jaroszynski, D.; Krushelnick, K.; Najmudin, Z. & Hooker, S. (2008). Laser-driven acceleration of electrons in a partially ionized plasma channel. *Physical Review Letters*, Vol. 100, p. 105005

Schlenvoigt, H.-P.; Haupt, K.; Debus, A.; Budde, F.; Jäckel, O.; Pfotenhauer, S.; Schwoerer, H.; Rohwer, E.; Gallacher, J. ; Brunetti, E.; Shanks, R. ; Wiggins, M. & Jaroszynski, D. (2008). A compact synchrotron radiation source driven by a laser-plasma wakefield accelerator. *Nature Physics*, Vol. 4, No. 2, pp. 130–133

Schlenvoigt, Hans-Peter (2009). *Synchrotron Radiation Sources driven by Laser Plasma Acclerators*, PhD thesis, IOQ Jena, www.physik.uni-jena.de/ioq

Schmid, K.; Veisz, L.; Tavella, F.; Benavides, S.; Tautz, R.; Herrmann, D.; Buck, A.; Hidding, B.; Marcinkevicius, A.; Schramm, U.; Geissler, M.; Meyer-ter-Vehn, J.; Habs, D. & Krausz, F. (2009). Few-Cycle Laser-Driven Electron Acceleration. *Physical Review Letters*, Vol. 102, p. 124801

Schreiber, J.; Bell, F.; Grüner, F.; Schramm, U.; Geissler, M.; Schnürer, M.; Ter-Avetisyan, S.; Hegelich, M.; Cobble, J.; Brambrink, E.; Fuchs, J.; Audebert, P. & Habs, D. (2006). Analytical model for ion acceleration by high-intensity laser pulses. *Physical Review Letters*, Vol. 97, p. 045005

Schwoerer, H.; Pfotenhauer, S.; Jäckel, O.; Amthor, K.-U.; Liesfeld, B.; Ziegler, W.; Sauerbrey, R.; Ledingham, K. & Esirkepov, T. (2006). Laser-plasma acceleration of quasimonoenergetic protons from microstructured targets *Nature*, Vol. 439, pp. 445–448

Sentoku, Y.; Cowan, T.; Kemp, A. & Ruhl, H. (2003). High energy proton acceleration in interaction of short laser pulse with dense plasma target. *Physics of Plasmas*, Vol. 10, No. 5, pp. 2009-2015

Snavely, R.A.; Key, M.H.; Hatchett, S.P.; Cowan, T.; Roth, M.; Phillips, T.W.; Stoyer, M.A.; Henry, E.A.; Sangster, T.C.; Singh, M.S.; Wilks, S.C.; MacKinnon, A.; Offenberger, A.; Pennington, D.M.; Yasuike, K.; Langdon, A.B.; Lasinski, B.F.; Johnson, J.; Perry, M.D. & Campbell, E.M. (2000). Intense High-Energy Proton Beams from Petawatt-Laser Irradiation of Solids. *Physical Review Letters*, Vol. 85, No. 14, pp. 2945–2948

Strickland, D. & Mourou, G. (1985). Compression of amplified chirped optical pulses. *Optics Communications*, Vol. 56, No. 3, pp. 219–221 Tajima, T. & Dawson, J. (1979). Laser electron-accelerator. *Physical Review Letters*, Vol. 43, No. 4, pp. 267–270

Ter-Avetisyan, S.; Schnürer, M.; Nickles, P.; Kalashnikov, M.; Risse, E.; Sokollik, T.; Sandner, W.; Andreev, A. & Tikhonchuk, V. (2006). Quasimonoenergetic deuteron bursts produced by ultraintense laser pulses. *Physical Review Letters*, Vol. 96, No. 14, p. 145006

Thomas, A.; Mangles, S.; Najmudin, Z.; Kaluza, M.; Murphy, C. & Krushelnick, K. (2007). Measurements of wave-breaking radiation from a laser-wakefield accelerator. *Physical Review Letters*, Vol. 98, p. 054802

Tikhonchuk, V.T.; Andreev, A.A.; Bochkarev, S.G. & Bychenkov, V.Y. (2005). Ion acceleration in short-laser-pulse interaction with solid foils. *Plasma Physics and Controlled Fusion*, Vol. 47, pp. B869-B877

van Tilborg, J.; Schroeder, C.; Filip, C.; Toth, Cs.; Geddes, C.; Fubiani, G.; Huber, R.; Kaindl, R.; Esarey, E. & Leemans, W. (2006). Temporal Characterization of Femtosecond Laser-Plasma-Accelerated Electron Bunches Using Terahertz Radiation. *Physical Review Letters*, Vol. 96, p. 014801

Toncian, T.; Borghesi, M.; Fuchs, J.; d'Humieres, E.; Antici, P.; Audebert, P.; Brambrink, E.; Cecchetti, C.A.; Pipahl, A.; Romagnani, L. & Willi, O. (2006). Ultrafast laser-driven microlens to focus and energy-select mega-electron volt protons. *Science*, Vol. 312, pp. 410–413
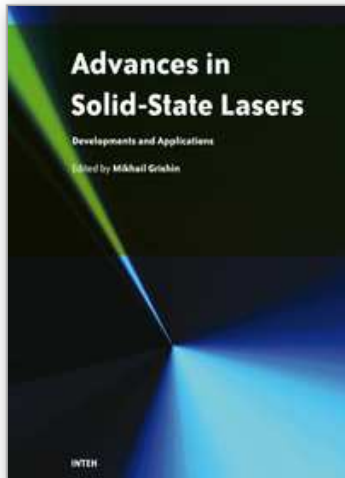
Advances in Solid State Lasers Development and Applications
Edited by Mikhail Grishin

Invention of the solid-state laser has initiated the beginning of the laser era. Performance of solid-state lasers improved amazingly during five decades. Nowadays, solid-state lasers remain one of the most rapidly developing branches of laser science and become an increasingly important tool for modern technology. This book represents a selection of chapters exhibiting various investigation directions in the field of solid-state lasers and the cutting edge of related applications. The materials are contributed by leading researchers and each chapter represents a comprehensive study reflecting advances in modern laser physics. Considered topics are intended to meet the needs of both specialists in laser system design and those who use laser techniques in fundamental science and applied research. This book is the result of efforts of experts from different countries. I would like to acknowledge the authors for their contribution to the book. I also wish to acknowledge Vedran Kordic for indispensable technical assistance in the book preparation and publishing.

How to reference
In order to correctly reference this scholarly work, feel free to copy and paste the following:

Hans-Peter Schlenvoigt, Oliver Jäckel, Sebastian M. Pfotenhauer, and Malte C. Kaluza (2010). Laser-based Particle Acceleration, Advances in Solid State Lasers Development and Applications, Mikhail Grishin (Ed.), ISBN: 978-953-7619-80-0, InTech, Available from: http://www.intechopen.com/books/advances-in-solid-state-lasers-development-and-applications/laser-based-particle-acceleration

INTECH
open science | open minds